

# Probabilistic Tsunami Hazard Analysis for Western Makran Coasts, Southeast Iran

**Hamid Zafarani**

International Institute of Earthquake Engineering and Seismology

**Leila Etemadsaeed** (✉ [etemadsaeed@iiees.ac.ir](mailto:etemadsaeed@iiees.ac.ir))

International Institute of Earthquake Engineering and Seismology <https://orcid.org/0000-0001-9150-0497>

**Mohammad Rahimi**

University of Tehran

**Navid Kheirdast**

International Institute of Earthquake Engineering and Seismology

**Amin Rashidi**

Savoie University: Universite Savoie Mont Blanc

**Yu-Lin Tsai**

National Central University

**Anooshiravan Ansari**

International Institute of Earthquake Engineering and Seismology

**Mohammad Mokhtari**

International Institute of Earthquake Engineering and Seismology

**Morteza Eskandari-Ghadi**

University of Tehran

---

## Research Article

**Keywords:** Tsunami, Makran subduction zone, Probabilistic hazard analysis, Heterogeneous slip distribution, Earthquake recurrence

**Posted Date:** February 4th, 2022

**DOI:** <https://doi.org/10.21203/rs.3.rs-1317527/v1>

**License:**  This work is licensed under a Creative Commons Attribution 4.0 International License.

[Read Full License](#)

---

# Probabilistic Tsunami Hazard Analysis for Western Makran Coasts, Southeast Iran

Hamid Zafarani<sup>1</sup>, Leila Etemadsaeed<sup>2</sup>, Mohammad Rahimi<sup>3</sup>, Navid Kheirdast<sup>1</sup>, Amin Rashidi<sup>4</sup>  
Yu-Lin Tsai<sup>5</sup>, Anooshiravan Ansari<sup>1</sup>, Mohammad Mokhtari<sup>1</sup>, Morteza Eskandari-Ghadi<sup>3</sup>

<sup>1</sup>International Institute of Earthquake Engineering and Seismology (IIEES), Tehran, Iran

<sup>2</sup>International Institute of Earthquake Engineering and Seismology (IIEES), Tehran, Iran, [Etemadsaeed@iiees.ac.ir](mailto:Etemadsaeed@iiees.ac.ir)

<sup>3</sup>School of Civil Engineering, College of Engineering, University of Tehran, Tehran, Iran

<sup>4</sup>LAMA UMR 5127 CNRS, Université Savoie Mont Blanc, Campus Scientifique, 73376, Le Bourget-du-Lac, France

<sup>5</sup>Graduate Institute of Hydrological Oceanic Sciences, National Central University, Taoyuan City, Taiwan

## Acknowledgment

The present study was carried out within the frame-work of the project "Tsunami and Seismic hazard assessment for the Makran region." Funding for this project was provided by the Plan and Budget Organization of the Islamic Republic of Iran (PBO). Our sincere thanks are due to the staff of this organization for their support: Dr. Javad Ghane-fard, Eng. Ali-Reza Totonchi, and Eng. Hamid-Reza Khashei.

# Probabilistic Tsunami Hazard Analysis for Western Makran Coasts, Southeast Iran

## Abstract

Makran subduction zone, along the southern coasts of Iran and Pakistan has a wide potential seismogenic zone and may be capable of generating large magnitude ( $M \sim 9$ ) tsunamigenic earthquakes. Considering ambiguities exist in tsunamigenic source characterization for subduction megathrusts like Makran, where detailed geologic, seismic, and geodetic data are insufficient, the probabilistic tsunami hazard analysis (PTHA) is the most prevalent approach to handle uncertainties and estimate more reliable tsunami hazard. Here, PTHA is performed for the coastal region of the western Makran, southeastern Iran. Using the logic tree approach, we have considered the uncertainty of maximum seismic magnitude, earthquake occurrence model, continuity of seismic zone, seismic coupling coefficient, depth of rupture, presence or absence of splay faults, fault locations, and fault slip distribution in PTHA calculation for the western Makran region. We have derived uniform tsunami hazard maps for two return periods of 475 and 2475 years for two confidence levels, the mean and the 84th percentile. Ground subsidence effects are also evaluated in a probabilistic manner. According to the PTHA results, Chabahar and Sirik towns are at the highest and lowest tsunami risk, respectively.

**Keywords: Tsunami, Makran subduction zone, Probabilistic hazard analysis, Heterogeneous slip distribution, Earthquake recurrence**

## 1- Introduction

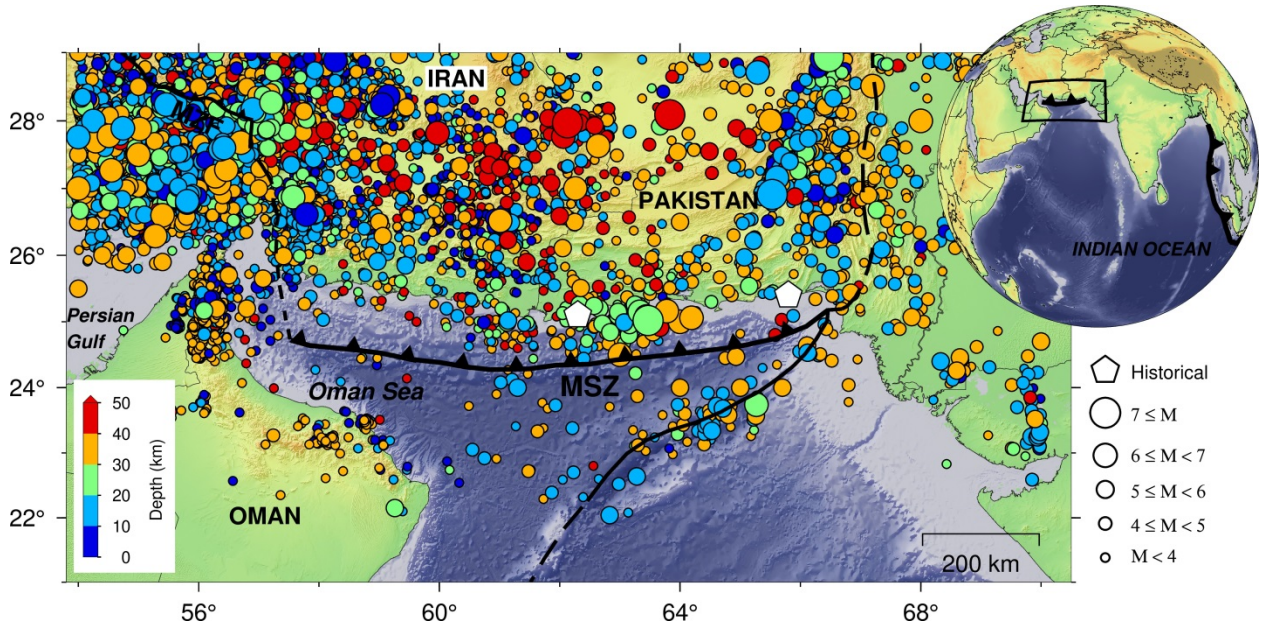
Taking into account the catastrophic consequences of recent large magnitude ( $M \sim 9$ ) tsunami-generating earthquakes (i.e., the 2004 Indian Sumatra–Andaman and the 2011 Japan Tohoku earthquakes); it is crucial to perform risk analysis studies for tsunami-prone regions. The first step for a risk analysis study is to conduct a tsunami hazard assessment to evaluate coastal tsunami heights from tsunamigenic source models.

There are two main approaches to perform a tsunami hazard assessment: deterministic and probabilistic. The deterministic approach is usually conducted for a formidable scenario that can pose the largest hazard to the region of interest. However, the deterministic technique might cause unanticipated errors, such as determining an inappropriate worst-case scenario (i.e., underestimated or overestimated). On the other hand, from an economic point of view, the assumption of a biggest or worst possible scenario might not be suitable for conventional design goals or strategies, as buildings and facilities have limited lifespans. Thus, a probabilistic tsunami hazard analysis (PTHA) considering in a comprehensive manner both epistemic (associated to our limited knowledge about things which are constant in time) and aleatory or inherent (associated to natural variations that occur between different events) uncertainties (Abrahamson and Bommer 2005) becomes a better option for a tsunami hazard assessment.

The Makran subduction zone (MSZ) (Fig. 1), formed by northward motion of Arabian plate beneath the Eurasia plate, has a historical catalog of large earthquakes and associated tsunamis (e.g., the Makran tsunami of 1945 with death toll near 4,000).

The MSZ is divided into two distinct segments, eastern and western Makran (Byrne et al. 1992). The eastern segment hosted several historical large magnitude events at 1765, 1810 and 1945 (Ambraseys and Melville 1982), but the western segment has been quiescent at least in the past 300 years. An ambiguous report of a large earthquake at 1483 was criticized by Musson (2009) and attributed to moderate shallow crustal earthquakes in the neighborhood regions. However, the possibility of a large earthquake on the western segment or a huge event resulting from a cascading rupture across two segments cannot be ruled out (Musson 2009). Penney et al. (2017), showed that the subduction interface in the western Makran may be locked, accumulating elastic strain, and move in megathrust earthquakes (see Frohling & Szeliga, 2016; Pajang et al., 2021), though its seismic coupling is reported to be weak (Ghadimi et al. 2021, submitted).

96 Recently, probabilistic tsunami hazard assessment of the MSZ has been a subject of interest for tsunami researchers  
97 and there are several PTHA for the Makran coastlines.



98  
99 **Fig. 1** Location of the MSZ and its seismicity. The pentagons show the historical earthquakes in this region. The circles show the  
100 occurred earthquakes from 1900 to 2019. The radius of a circle presents the magnitude of an earthquake. The color shading  
101 indicates the focal depths in km

102 A list of these studies and their specifications is summarized in Table 1. They have been conducted at different  
103 scales of global, regional and local and different levels of detail were applied to describe the subduction geometry,  
104 fault slip distribution and other technical factors. A major drawback of some of these studies is that the seismicity rate  
105 was used instead of long-term fault slip rate to constrain the recurrence rates in the Gutenberg-Richter (GR) model  
106 (see section 2-2). Moreover, they ignored the important uncertainties regarding the recurrence model or Maximum  
107 magnitude and updip rupture depth.

108 The first PTHA research for Makran was conducted by Burbidge et al. (2009). They produced probabilistic tsunami  
109 hazard maps for the Indian Ocean countries, including Iran, considering the effects of tsunamis generated by the  
110 Makran, Sumatra–Andaman, and South Sandwich subduction zones. They presented their results as annual  
111 probabilities of exceeding certain tsunami wave amplitude in the water depth of 100 m. Although not explicitly  
112 mentioned, it seems that the coupling factor in this study has been taken into account with the technique in which the  
113 rate of earthquake occurrence for each subduction zone is determined based on the percentage of the global subduction  
114 seismicity. Activity rates for each subduction zone, defined as the fraction of the global subduction zone seismicity  
115 that would be expected on each zone, was calculated based on the ratio of its length to the length of all tsunamigenic  
116 subduction zones in the world. The main problem in this technique is the assumption that the coupling factor for any  
117 given subduction zone is not significantly different from the global average along megathrusts In Burbidge et al.  
118 (2009) study, three possible rupture areas were considered for each modeled earthquake using the empirical scaling  
119 relations of Wells and Coppersmith (1994), which is not a subduction zone-specific relationship.

120 Following the study of Burbidge et al. (2009), several articles have been conducted on the PTHA in the MSZ.  
121 Using a limited mixed earthquake catalog of the Makran region including shallow crustal, interface and intraplate  
122 events to constrain the truncated Gutenberg-Richter (TGR) recurrence relation, Heidarzadeh and Kijko (2011) defined  
123 three scenarios with identical fixed magnitude ( $M_w$  8.1) in the eastern, central and western Makran for a probabilistic  
124 tsunami hazard assessment along the coasts of Iran, Oman and Pakistan. They considered fixed magnitude, location,  
125 and depth and also uniform slip distribution for each scenario.

126 Løvholt et al. (2012) conducted a tsunami hazard assessment on the global scale including the MSZ. Hoechner et  
127 al. (2016) used the TGR recurrence model and Makran instrumental era catalog in computing the exceedance rate of

128 tsunami height for Makran coastlines. The slip rate of the MSZ was ignored in their analysis and they used the general  
129 seismicity of the whole Makran region without any distinction between shallow crustal, interface and intraplate  
130 earthquakes.

131 El-Hussain et al. (2016, 2018) constructed some source models with different magnitudes along the MSZ and  
132 used the logic-tree procedure and probabilistic method to estimate the tsunami hazard along the Oman shorelines.  
133 They only employed the TGR recurrence model for magnitude-frequency and assumed uniform slip on earthquake  
134 sources. Also, while not considering the coupling coefficient, probabilistic results were presented for the coasts of  
135 Oman.

136 In another global-scale study, Davies et al. (2017) performed a probabilistic tsunami hazard assessment. They  
137 assigned three slip rates of 5.4, 9.0 and 13.0 mm/year for the Makran fault. Assuming a convergence rate of 20  
138 mm/year, the resulting coupling factors are about 0.3, 0.5 and 0.7. They also assumed three maximum magnitudes of  
139 8.1, 8.8 and 9.5. They did not take into account the segmentation of the MSZ into the western and eastern segments.

140 Another probabilistic tsunami hazard assessment was done by Am. Rashidi et al. (2020b) for a range of  
141 heterogeneous slip distributions of the MSZ. Tsunami hazard curves and probability maps for the region were their  
142 outcome. They used the TGR recurrence model and a fixed non-planar geometry for the MSZ. The effect of seismic  
143 coupling was not a part of their computations.

144 In general, probabilistic tsunami hazard assessment is a multidisciplinary problem which contains tsunami  
145 numerical modeling and probabilistic calculations for the earthquake source and tsunami wave amplitude. This would  
146 require different experts in various fields of seismology, seismotectonics, geodesy, probability and statistics, hazard  
147 assessment, and numerical hydrodynamic modeling. So far, a comprehensive study using the knowledge of the above  
148 various fields and combining them together in a logical and scientific format, has not been done at a regional-scale for  
149 the western Makran coastline. Present study tries to resolve and address the weaknesses and limitations of the previous  
150 studies as much as possible.

151 In this study, we consider the uncertainty of maximum seismic magnitude, earthquake occurrence models,  
152 continuity of seismic zone, seismic coupling coefficient, depth of rupture, presence or absence of splay faults, fault  
153 locations, and fault slip distribution in PTHA for the MSZ. To clarify the importance of considering these  
154 uncertainties, it is worth noting that in modeling the tsunami observed after the only instrumental era large interface  
155 event in this region, i.e. the 1945 Makran earthquake with a magnitude of 8.1, there are significant differences between  
156 the hypotheses of various studies (e.g., Heidarzadeh et al. 2008, 2009; Jaiswal et al. 2009; Neetu et al. 2011).  
157 Considering homogeneous slip model, and presence or no presence of splay faulting (reaching the rupture to the  
158 seabed), are among the main reasons for the failure to model the observed tsunami wave height of this earthquake.  
159 This would place another emphasis on the key role of nonhomogeneous slip distribution to have a more reliable  
160 estimate of expected tsunami wave amplitudes, a factor that was ignored in most of the past PTHA studies (Table 1).  
161 In addition to non-uniform slip, the present study incorporates multiple assumptions including different top depths of  
162 the rupture, fault-rupture-scaling model, the effect of coupling in seismic activity of the region, and a more precise  
163 bathymetry data (see sections 2). Earth subsidence effects are also evaluated in a probabilistic manner in this study for  
164 the first time.

165 It should be mentioned that our study only includes earthquake scenarios from the MSZ. As shown by the  
166 simulation results in Okal and Synolakis (2008), far-field scenarios have only mild effects on the Makran coasts and  
167 are thus excluded from our study.

168

## 169 **2- Uncertainties in western Makran tsunami modeling**

170 There are both aleatory and epistemic uncertainties in a PTHA study, though sometimes the margin between these  
171 two categories is vague and depends on personal opinion.

172 Aleatory uncertainties in fact indicate the natural randomness inherent in the nature of phenomena, whereas  
173 epistemic uncertainties are due to a lack of information and human knowledge about the natural processes. The logic  
174 tree is an efficient tool for considering epistemic uncertainties in probabilistic hazard and risk analysis studies, first  
175 introduced to the field by Kulkarni et al. (1984). One of the most important parameters in determining the behavior

176 and output of the logic tree is the weighting done by experts into its various branches, which represent different  
177 hypotheses in modeling. The branch weights in a logic tree represent the degree of belief of experts in each element  
178 of models.

179 In the next section, by expression the uncertainties in tsunami hazard analysis in the MSZ; the considered logic  
180 tree for this study (Fig. 2) is introduced. It should be noted that, the dip-angle of the subduction interface of the MSZ  
181 could be another source of uncertainty and was a matter of debate for a long time (see e.g. Byrne et al. (1992), Maggi  
182 et al. (2000), Kopp et al (2000), Penny et al. (2017)). Penny et al. (2017) implemented well-located earthquakes in the  
183 region, and receiver functions from local seismometers to constrain the range of possible interface dips. They reported  
184 maximum average dips of  $\sim 11^\circ$  in the western,  $\sim 9^\circ$  in the central and  $\sim 8^\circ$  in the eastern Makran region, respectively.  
185 In a recent study, using the wide-angle reflection technique along three crustal-scale, trench-perpendicular, deep  
186 seismic sounding profiles, Haberland et al. (2020) has delineated the position and the dip of the subducting plate  
187 (oceanic Moho). According to Haberland et al. (2020) the crustal structure and the very gentle dip ( $\sim 8^\circ \pm 2^\circ$ ) of the  
188 subducting plate suggest a very wide contact zone, potentially allowing very wide asperities. In the light of  
189 aforementioned studies, here a fixed value is used for the dip of the subduction interface which is important for  
190 assessing tsunami wave height generated by different seismic scenarios.

191

## 192 **2-1 Maximum seismic magnitude of the MSZ**

193 For years, seismologists believed that some subduction zones would never be able to produce earthquakes of  
194 magnitude Mw 9.0 or greater (Ruff and Kanamori 1980). However, after the 2004 Indonesia Mw 9.2 and the 2011  
195 Japan Mw 9.0 earthquakes, the general view of seismologists is that all or at least most of the subduction zones are  
196 capable to produce an earthquake of magnitude Mw 9.0, in a global analogy context. Generally, there are two main  
197 approaches for determination of the maximum magnitude ( $M_{max}$ ): those that are based on an earthquake catalog  
198 (maximum observed magnitude plus an increment) and those based on empirical scaling relations through a seismic  
199 source zone model. The second method, in the simplest way uses fault length, while a more accurate alternative is to  
200 use the rupture area (which is proportional to the accumulated moment, Hanks and Kanamori 1979). Due to lack of  
201 historical events, except the 1945 Mw 8.2 earthquake in the eastern Makran, here we emphasize more on the second  
202 approach, which implies adopting the concept of global analogy of  $M_{max}$  for all subduction zones (Meletti et al.  
203 2010). As the seismic moment released in an earthquake is a function of rupture area, so assuming an average shear  
204 modulus of  $\mu = 30$  GPa for subduction zones (Hanks and Kanamori 1979), average dip angle of  $8^\circ$  and length of 900  
205 km for the entire MSZ (or even the eastern or western segment of the MSZ), occurrence of an earthquake magnitude  
206 equal to or greater than Mw 9.0 is possible.

207 Moreover, thermal modeling performed by Smith (2012) to determine areas with temperatures above  $150^\circ\text{C}$  in  
208 sediments, showed that the occurrence of earthquakes with magnitude up to Mw 9.2 in the MSZ is possible. According  
209 to the Smith's (2012) modeling, the Makran crust reaches a temperature of  $350^\circ\text{C}$  at a depth of 60 km and a temperature  
210 of  $450^\circ\text{C}$  at a depth of 75 km. Therefore, with a length of about 800 km and a rupture width of about 200–350 km, a  
211 magnitude Mw 9.0 to 9.2 is proposed as the maximum magnitude of the MSZ in the worst-case scenario. In another  
212 study, by modeling deformation based on the GPS data to determine the downdip locking width, Frohling and Szeliga  
213 (2016a) proposed a maximum magnitude of Mw 8.8 for the entire length of the MSZ. Also, considering the length of  
214 more than 900 km for the MSZ and using empirical scaling relationships specific to subduction zones, such as that  
215 proposed by Skarlatoudis et al. (2016), occurrence of earthquakes with a magnitude of about Mw 9.1–9.2 is probable  
216 in the MSZ.

217 On the other hand, study of the location of megathrust subduction earthquakes shows that earthquakes with a  
218 magnitude of Mw 9.0 and more occurred in places such as the MSZ that have previously experienced quiescent periods  
219 with few numbers of moderate earthquakes (Hort et al., 2011).

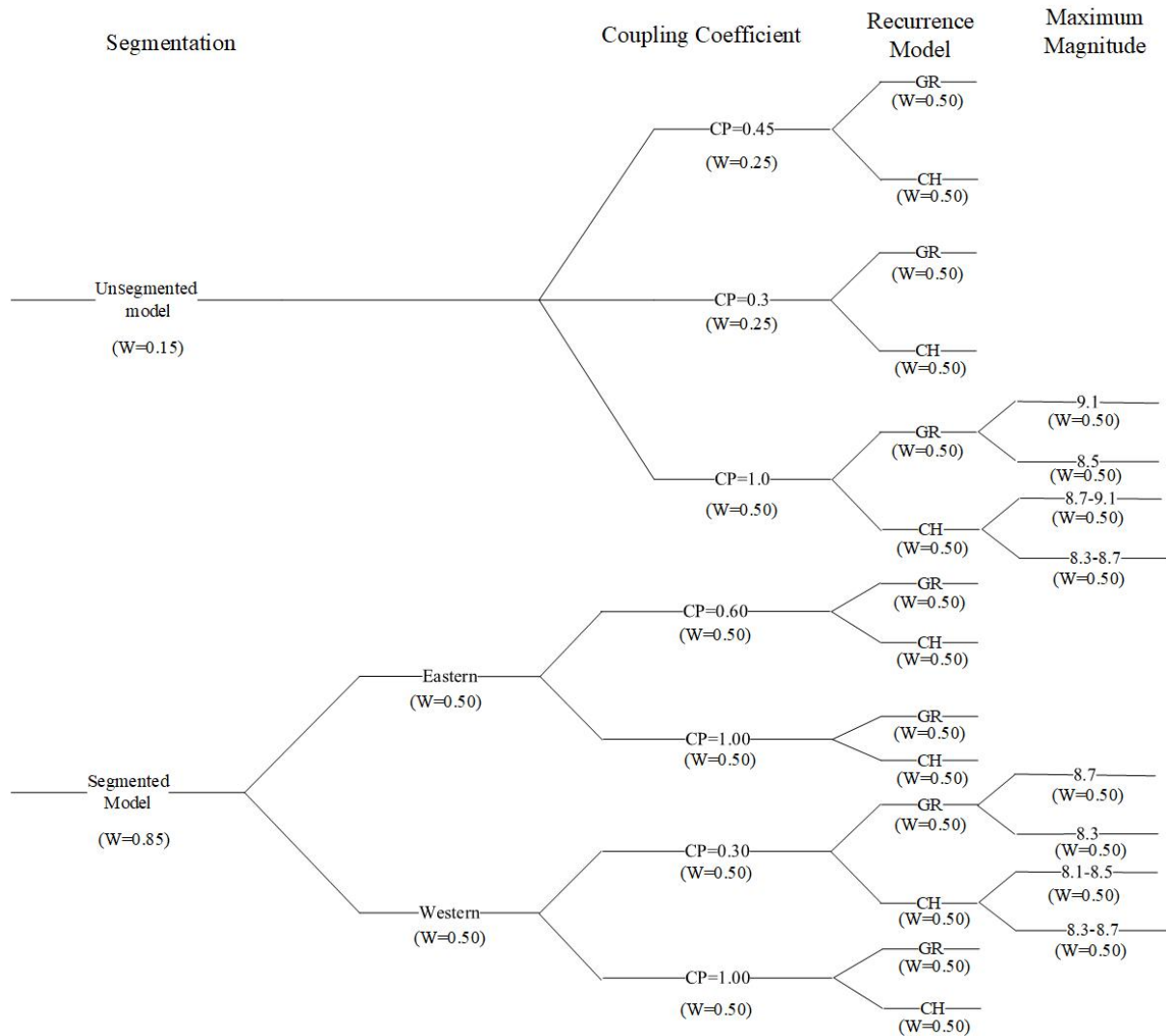
220 In a recent two-dimensional numerical study of megathrust earthquakes in subductions (magnitude greater than  
221 Mw 8.5), Muldashev and Sobolev (2020) showed that the dip angle of the subduction plate has the greatest effect on  
222 the maximum expected magnitude of a subduction zone. Hence, the lower the dip angles of the subduction zone, the

223 greater potential for producing larger megathrust earthquakes. Therefore, taking into account low dip angle ( $\sim 8^\circ$ ) of  
224 the subduction plate in the MSZ, there is potential for occurrence of larger megathrust earthquakes.

**Table 1.** A summary of PTHA studies conducted for the MSZ

Study	Output(s)	Modeling	Slip distribution	Bathymetry resolution	Magnitude Range	Fault scaling relationship	Earthquake recurrence model	Coupling	Scale of study
Burbidge et al. (2009)	Tsunami wave amplitudes in water depth of 100 m	Linear shallow water wave equations (URSGA model)	Uniform	2 arc min	7.0 – 8.2 and 9.1	Wells and Coppersmith (1994)	TGR	Average coupling for global subduction zones	Global
Heidarzadeh and Kijko (2011)	Tsunami wave amplitudes at coastline	Nonlinear shallow water wave equations (TUNAMI-N2 model)	Uniform	1 arc min	8.1	The 1945 Makran earthquake	TGR	Not included	Regional
Løvholt et al. (2012)	Tsunami wave amplitudes at coast (water depth of 0.5 m) computed using amplification factors from water depth of 50 m	Linear shallow water wave equations (GloBouss model)	Uniform	2 arc min	Up to 8.4	Wells and Coppersmith (1994)	TGR	Not included	Global
El-Hussain et al. (2016)	Tsunami wave amplitudes at coastline	Nonlinear shallow water wave equations (NSWING model)	Uniform	30 arc sec	7.9 – 9.1	-	TGR	Not included	Local
Hoechner et al. (2016)	Tsunami wave amplitudes at coast (water depth of 1.0 m) computed based on Green's law from amplitudes in water depth of 50 m	Linear shallow water wave equations (easyWave model)	Non-uniform	30 arc sec	Up to 9.0	Blaser et al. (2010)	TGR	Not included	Regional

Study	Output(s)	Modeling	Slip distribution	Bathymetry resolution	Magnitude Range	Fault scaling relationship	Earthquake recurrence model	Coupling	Scale of study
El-Hussain et al. (2018)	Tsunami wave amplitudes at coastline	Nonlinear shallow water wave equations (NSWING model)	Uniform	30 arc sec	7.5 – 8.8	-	TGR	Not included	Local
Davies et al. (2017)	Tsunami wave amplitudes at coast (water depth of 0.5 m) computed using amplification factors and Green's law from amplitudes in water depths of 100 m	Linear shallow water wave equations (URSGA model)	Uniform	30 arc sec	7.5 – 8.1 8.8 – 9.5	Strasser et al. (2010)	TGR	Different scenarios are considered	Global
Am. Rashidi et al. (2020b)	Tsunami wave amplitudes at coastline	Nonlinear shallow water wave equations (COMCOT model)	Non-uniform	30 arc sec	9.06 – 9.12	Smith et al. (2012)	TGR	Not included	Regional
This study	Tsunami wave amplitudes at coast (water depth of 0.5 m) computed based on Green's law from amplitudes in water depths of 10 and 50 m	Nonlinear shallow water wave equations (COMCOT model)	Non-uniform	15 arc sec (3 arc sec for some areas)	7.7 – 9.1	Skarlatoudis et al. (2016)	TGR, Pure Characteristics model	Computed and different scenarios are considered	Regional



229  
230

231

Fig. 2 The logic tree used in this study

232 Many earthquakes have been reported compared to smaller ones. Despite the extensive data for attempts have  
 233 been made to obtain empirical scaling relationships between fault rupture dimensions and seismic magnitude  
 234 based on past earthquakes data (Papazachos et al. 2004; Blaser et al. 2010; Strasser et al. 2010; Murotani et al.  
 235 2013; Skarlatoudis et al. 2016; Allen and Hayes 2017; Thingbaijam et al. 2017). One of the important points is  
 236 whether the scaling relations, which are mainly constrained and developed by using smaller earthquake data, can  
 237 also be attributed to megathrust earthquakes in subduction zones, while different characteristics of these large  
 238 earthquakes in subduction zones, there is still low data to determine the rupture behavior of giant earthquakes  
 239 (magnitude greater than 8.5). This limitation is especially evident in determining the width of the rupture plate  
 240 (Skarlatoudis et al. 2016). Some researchers suggest rupture width saturation, meaning that the fault width does  
 241 not change with increasing the earthquake magnitude after a certain value (Tajima et al., 2013; Skarlatoudis et al.,  
 242 2016). However, the lack of data in this range of magnitude makes it difficult to draw final conclusions.

243 According to Strasser et al., (2010) it is important to consider more than one empirical scaling relationship to  
 244 determine maximum magnitude from an epistemic uncertainty perspective. Therefore, in this study the possible  
 245 maximum earthquake magnitude has been calculated with three scaling relationships of Skarlatoudis et al. (2016),  
 246 Thingbaijam et al. (2017) and Allen and Hayes (2017), based on different assumptions regarding the fault rupture  
 247 length, width and area.

248 These three selected relations have considered more earthquakes than the other existing scaling relations,  
 249 including very large recent earthquakes (for example, the 2011 Tohoku earthquake) and therefore are more reliable  
 250 in this respect.

251 In this study, the selected scaling relationships are used with equal weight in determining the maximum  
 252 magnitude for the MSZ based on the width, length and area of the rupture plate as follows:

- 253 - Empirical scaling relationships based on magnitude-rupture area (considering two rupture area scenarios).
- 254 - Empirical scaling relationships based on magnitude-rupture width (considering two rupture width scenarios).
- 255 - Empirical scaling relationships based on magnitude-rupture length.

256 Therefore, if the rupture width (width of the locked area) is assumed between 80 km (minimum depth of 14  
 257 km and maximum depth of about 25 km) and 185 km (minimum depth of 14 km and maximum depth of about  
 258 40-45 km), based on the selected empirical scaling relationships of subduction zones, the maximum possible  
 259 magnitude for the two pessimistic and optimistic scenarios in each of the western, eastern and entire Makran logic  
 260 tree branches will be (8.7, 8.7, 9.1), (8.3, 8.3, 8.5), respectively. In this regard, the maximum moment magnitude  
 261 in the GR models and the central magnitude in the pure characteristic model for each of the western, eastern, and  
 262 entire Makran logic tree branches are selected equal to these values.  
 263

## 264 2-2 Earthquake occurrence model

265 In a PTHA study, an empirical model that gives the number of earthquakes with magnitude  $m$  that occur within  
 266 a year is needed to explain the magnitude-frequency distribution of earthquakes. In earthquake hazard studies,  
 267 either the GR or the Characteristic-Earthquake models are commonly used. As pointed out by Davis et al. (2017),  
 268 two modified version of GR models, that incorporate a maximum magnitude bounds are often used to characterize  
 269 earthquake recurrences:

270 The Characteristic GR (Kagan 2002) as:

$$271 \text{GR}(m_w) = f(x) = \begin{cases} 10^{a-bm_w}, & m_{w,min} \leq m_w \leq m_{w,max} \\ 0, & m_w > m_{w,max} \end{cases} \quad (1)$$

272 And the TGR as:  
 273

$$274 \text{GR}(m_w) = \begin{cases} 10^{a-bm_w} - 10^{a-bm_{w,max}}, & m_{w,min} \leq m_w \leq m_{w,max} \\ 0, & m_w > m_{w,max} \end{cases} \quad (2)$$

275 In the PTHA studies, the first model is usually called the Characteristic model since, like the well-known  
 276 Characteristic model of seismic hazard studies (Youngs and Coppersmith 1985), its recurrence rate at  $M_{max}$  is  
 277 not exactly zero. On the other hand, the second model (i.e. TGR), also known as the exponential model, has a  
 278 recurrence rate at  $M_{max}$ , that is exactly zero.  
 279

280 The Characteristic model, also known as the "Maximum magnitude" model generates earthquakes only within  
 281 a relatively narrow magnitude range (Stewart et al. 2002). As earthquakes of small to moderate magnitude that  
 282 follow the GR distribution are unlikely to cause a tsunami (Thio et al (2007)) in addition to the TGR model, we  
 283 also use a pure Characteristic model described above.

284 The Characteristic model is more consistent with the observed seismicity of the Makran region (lack of  
 285 moderate to large events) and also does not require a b-value (see section 2-3). This is important from the  
 286 viewpoint that some recurrence intervals resulted from a GR model, such as one earthquake with  $M \geq 7.5$  every  
 287 30 years, which are reported by El-Hosseini et al. (2016), cannot be validated at least through the last 200 years  
 288 (Ambraseys & Melville, 1982).

289 A pure characteristic recurrence model with a width parameter of 0.3-0.5 magnitude units (depending on the  
 290 past seismicity) was used in a probabilistic Tsunami hazard study in Japan, representing characteristic earthquakes  
 291 with a uniform distribution (Annaka et al. 2007).

292 Because only earthquakes with magnitudes greater than 7.5 can generate tsunamis, Thio et al. (2007) in another  
 293 study on the probabilistic hazard of tsunamis in eastern Asia, rely solely on the pure Characteristic models. A  
 294 similar study is linked to what is known as quiescent seismicity in the Cascadia region of eastern Canada and

295 United States, where the GR model was not used; however, the recurrence model for the interface earthquakes  
296 was recognized as a pure characteristic model with a return period of 500 years for a M>9 event and a return  
297 period of 100 years for a M>8 event (Frankel et al. 2002).

298 Atkinson and Goda (2011) used an alternative version of pure Characteristic recurrence model, assuming a  
299 normal distribution with a mean of 8.5 and a standard deviation of 0.5 to calculate the recurrence rates for various  
300 moment magnitudes of the Cascadia subduction zone.

301 To constrain the recurrence models using fault slip rates, the following relationship between the annual rate of  
302 moment-release and earthquake recurrence rates is suggested by Anderson and Luco (1983):

303

$$\dot{M}_0 = \mu AS = \int_{m_{min}}^{M_{max}} M_0(m) \dot{n}(m) dm \quad (3)$$

304

305 Where  $\dot{n}(m)$  is the density function for earthquake occurrence rate,  $\dot{M}_0$  denotes the annual rate of moment-  
306 release, and  $M_0(m)$  denotes the magnitude-seismic moment relationship proposed by Hanks and Kanamori  
307 (1979):

308

$$M_0(m) = 10^{1.5m+9.05} \quad (4)$$

309

310 It is worth noting that both the GR and the Characteristic models were favored in different studies when  
311 deciding on a recurrence model (Schwartz 1999; Pisarenko and Sornette 2004).

312

### 313 **2-3 b-value in Gutenberg–Richter model**

314 Following the discussion above, two recurrence models, namely the TGR and the pure Characteristic model  
315 (also referred to as Maximum magnitude recurrence model) are used in the current study. Therefore, to completely  
316 explain the seismicity in the Makran subduction region, we must obtain the b-value.

317 According to (Benito et al. 2012), in any subduction zone, three seismicity regimes, crustal, interface slab, and  
318 inslab, can cause earthquakes. In the Makran region, the lack of interface slab earthquakes is a significant  
319 limitation to using the GR recurrence relation. Unfortunately, due to a lack of data, seismicity parameters in the  
320 subduction zone are normally calculated using a combination of interface, inslab and crustal earthquakes. For  
321 example, Deif and El-Hussain (2012) and Hoechner et al (2016), combined earthquakes from all three seismic  
322 regimes and estimated the b-value to be 0.77 and 0.82, respectively.

323 Another issue caused by the lack of earthquakes, as emphasized by Pisarenko and Sornette (2004), is weak  
324 constraint at the end tail of the GR distribution, where major tsunamigenic events occur. It's worth noting that the  
325 aforementioned issues also exist in other subduction zones, such as the Cascadia subduction zone, where seismic  
326 activity is currently low.

327 Since the lack of seismic activity prevents the calculation of the b-value in the Cascadia area, in a  
328 comprehensive study by BC Hydro (2012), its value was adopted from other studies around the world where the  
329 abundance of seismicity permits the calculation of the b-value. The absence of interface seismic data and the  
330 presence of a thick sediment layer (McAdoo et al. 2004) are common features of both the Cascadia and Makran  
331 subduction zones.

332 According to the GEM Faulted Earth Subduction Interface Characterization Project: Version 2.0 (Berryman  
333 et al. 2015), who processed seismicity data from subduction zones around the world and took into account the low  
334 rate of M>5.5 earthquakes in Hikurangi, the Caribbean, Cascadia, and Makran, they suggested that the b-value  
335 for the interface slab in these regions is likely lower than the global average.

336 By reviewing the b-values reported world-wide, Wang et al (2016) allocated 0.7 to the north Taiwan  
337 subduction zone, Power et al (2013) used 0.75 for the Japan Trench, and GEM group (Berryman et al. 2015) used  
338 a range of 0.7-1.2 for subduction zones around the world. Note that in the GEM report, the b-value in Makran was  
339 assigned according to Bayrak et al (2002) who devised the b-value equal to 0.78. However, the combination of  
340 Zagros (a shallow crustal environment) and Makran earthquakes, which was disregarded in the GEM report, is a  
341 serious criticism of Bayrak et al (2002).

342 We calculated the b-value by reviewing previous global studies and gathering seismic activity in the western  
343 and eastern MSZs. We obtained a b-value of 0.75 without distinguishing between shallow crustal and interface  
344 slab regimes, but excluding inslab events (Ah. Rashidi et al., 2020).

#### 345 **2-4 Continuity of seismic zone**

346 The MSZ is an area with an approximate length of 1000 km which has been extended through the coast of Iran  
347 & Pakistan from Strait of Hormuz to Karachi in Pakistan. According to (Heuret et al. 2011), when the length of  
348 subduction is below ~500 km, the large earthquakes is unlikely to happen. However, the observed amount of  
349 rupture length in past-longer subduction earthquakes was also limited to part of the total length of the subduction  
350 zone (500~2000 km). The reason for this discontinuity in rupture propagation, and consequently the limited  
351 rupture length, is that the complexity of the subducting plate (such as different sediment thicknesses, fracture  
352 zones, Seamounts, the presence of horst and Graben) and the strength of the upper plate cause local changes in  
353 friction along the length.

354 Although there are strong evidences of the segmentation of the MSZ into two parts, eastern and western, with  
355 different geodynamic behaviors (Byrne et al. 1992), the possibility of a very large earthquake due to the cascading  
356 rupture of both segments could not be ignored, assuming the rupture spreads from the west to the east or vice  
357 versa. Therefore, it is necessary to consider the MSZ as an integrated seismic region, although not very likely, in  
358 order to consider all possible scenarios for thorough tsunami hazard estimation.

359 In previous researches conducted, such as the tsunami hazard analysis for the coasts of Oman ( El-Hussain et  
360 al., 2016), an integrated rupture in Makran with a magnitude of more than 9.0 with a branch weight of 0.15 has  
361 been considered. Also, in the seismic hazard analysis report of the cities of Abu Dhabi, Dubai and Ras-al-Khaimah  
362 in the United Arab Emirates (Aldama-Bustos et al. 2009), a weight of 0.05 is attributed to the scenario  
363 corresponding to the cascading rupture of the MSZ.

364 In present study, taking into account the above discussion a logic tree branch with a low weight (0.15) is  
365 considered to account for the possibility of a cascading rupture along two MSZ segments (the unsegmented branch  
366 in the logic tree of Fig. 2).

#### 367 **2-5 Seismic coupling coefficient**

368 The seismic coupling coefficient  $\chi_s$  is the ratio of seismic moment released by earthquakes to seismic moment  
369 stored between plates as a result of relative tectonic movement within a subduction zone.

370 The seismic moment rate is generally calculated by dividing the total seismic moment obtained from recorded  
371 earthquakes in an instrumental catalogue by the catalogue's time period. It is worth noting that the estimation of  
372 seismic moment rate is inherently uncertain due to the long return periods of major earthquakes that might not be  
373 reported in instrumental catalogues. Actually, a century of seismic activity in a subduction zone does not  
374 adequately represent the long-term seismicity, and the approximation based on it, results in lower coupling  
375 coefficients. Taking into account the scarcity of seismicity in the Makran region, seismic coupling of the MSZ is  
376 another open question.

377 The measurement of the inter-seismic strain accumulation rate, which gives the inter-seismic moment rate  
378 ( $X_g$ ), has been easily accomplished due to the rise in the number of GPS stations (Scholz and Campos (2012)).  
379 The shortcomings of the traditional catalogue-based method for calculating the seismic coupling rate, which is  
380 primarily due to the lack of large earthquakes recorded in seismic catalogues, have been resolved by the novel  
381 geodetic approach. Note that although the coupling ratio calculated by the classical approach yields the released  
382 moment, the geodetic coupling rate gives the total energy stored within the tectonic plates. Both methods are equal  
383 in the long run if the coupling rate remains constant over time. The inconsistency between the two concepts  
384 discussed above highlights earthquakes that have been ignored in seismic catalogues and should be explored  
385 further using historical resources or paleo-seismic methods (Scholz and Campos (2012)). One source of  
386 uncertainty in the estimation of coupling rate is the error in the approximation of coupled surface area ( $A_c$ ), which  
387 is the region of the contacting plates where seismic slip occurs (seismogenic area). The length of this area ( $L_c$ ) is  
388 inferred from the length of the subducting segment. However, the end pieces from both sides are often ignored. A  
389 more important source of uncertainty is the estimation of the coupled area's width ( $W_c$ ).  $W_c$  is determined between  
390 the accretionary wedge and the brittle-plastic transition zone. According to Scholz and Campos (2012), the brittle-

393 plastic transition normally occurs where the temperature reaches 350°C. Another transition zone exists below this  
394 temperature, which is where slow-slip events usually occur. Further below, the plates can freely slip without any  
395 coupling.

396 There are three ways to calculate the width of the coupled field,  $W_c$ . First, by observing the location of back-  
397 ground seismic activity, second, based on the slipped areas of large previous earthquakes, and third, by inverting  
398 the GPS data

399 The first two methods have a 30 percent uncertainty (Scholz and Campos 2012), while the third method has a  
400 lower uncertainty and is more effective in determining the deep seismic edge. Because the top seismic edge is  
401 usually located far from the coast and the GPS stations are located along the coast, the data provided by the GPS  
402 stations does not provide a good constraint for the top edge depth. Scholz and Campos (2012) used both GPS data  
403 and seismological observations to calculate the amount of seismic coupling in many subduction zones around the  
404 world. According to their study, the coupling rate is between 0 and 1, with an average value of 0.6.

405 In the other study, Heuret et al. (2011) reported the coupling coefficient based only on the previous century  
406 seismicity, and the slip-rate values across the subducting area. It is worth noting that Heuret et al (2011) used a  
407 shear modulus of  $G=50$  GPa instead of the more common values of  $G=30$  GPa (Hanks and Kanamori 1979; Davies  
408 et al. 2017) or  $G=40$  GPa (Scholz and Campos 2012), which resulted in a 20% reduction in the coupling coefficient  
409 values compared to what was reported by Scholz and Campos (2012). The seismic coupling by Heuret et al. (2011)  
410 was found to be uncorrelated ( $R = 0.17$ ) with the subduction velocity, which is consistent with the observation of  
411 Pacheco et al. (1993).

412 In a comprehensive study by GEM group (Berryman et al. 2015), the coupling ratio in the MSZ was assumed  
413 to be between 0.3 and 0.7. Note that in (Berryman et al. 2015) the coupling ratio was based on expert opinion  
414 rather than modelling. As emphasized by Byrne et al (1992), because the creeping regime exists at every  
415 subduction zone, we assumed two low and high creeping branches for both eastern and western Makran.  
416 Furthermore, the fact that some faults have a cycle of seismic activity and silence was taken into consideration  
417 when assessing branch weights .

418 Davies et al. (2017) considered subduction rate as 19 mm/yr and used three different seismic slip rates of 5.4,  
419 9.0, and 13.0 mm/yr, corresponding to coupling rates of 0.3, 0.5, and 0.7, respectively. Furthermore, maximum  
420 magnitudes of 8.1, 8.8, and 9.5 were assumed, accordingly.

421 Ghadimi et al. (2021, submitted.) computed the long-term crustal flow and forecast of seismicity for the MSZ,  
422 using a kinematic finite element technique. They investigated the possibility of creep in western Makran, by  
423 comparing two different models with the coupling rates of 0 (means free slipping) and 1 (corresponds to a totally  
424 locked fault) for the western Makran. The results of the temporarily locked model indicated about 1~3 mm/yr  
425 higher rate of shortening than the other models with the steady creeping subduction. Also, the predicted  
426 interseismic velocities and seismicity from the creeping model are more accurate for the western Makran.

427 In this article, based on the results of Ghadimi et al. (2021, submitted) and the review presented above, we  
428 used a coupling ratio of 0.3 for western, 0.6 for eastern, and two values of 0.3 and 0.45 for an unsegmented model.  
429 Additional conservative branches are also included in the logic tree for the eastern, western, and unsegmented  
430 model, with a pessimistic coupling coefficient of 1.0, indicating a fully coupled subduction (Fig. 2)

431

## 432 **2-6 Updip rupture depth**

433 The shallow aseismic-seismic transition depth ( $d_s$ ) estimated by Pacheco et al. (1993) as  $d_s = 10$  km for all  
434 subduction zones, was adopted by the Slab1.0 Model (Hayes et al. 2012). Slab 2.0. (Hayes et al. 2018) takes a  
435 different approach based on the seismicity depth of subduction zones, with a minimum  $d_s = 9$  km (Tonga  
436 subduction zone), a maximum  $d_s = 16$  km (Kamchatka subduction zone), and an average  $d_s = 12$  km. In contrast to  
437 other active subduction zones around the globe (Smith et al. 2012), the MSZ has a thick sediment layer (3-7 km)  
438 (McAdoo et al. 2004), so an active depth deeper than the global average seems reasonable. For the MSZ,  
439 considering the limited seismic data obtained in the subduction interface, Slab 2.0 (Hayes et al. 2018) reports  
440 shallow and deep seismogenic depths of 13 km and 40 km, respectively. Taking into account the above discussion  
441 and considering depth distribution of local seismicity in the region (Ah. Rashidi et al., 2020) (Fig. 3), the updip  
442 rupture depth in Makran has been set at 14 km as an optimistic value.

443 Prior to the Indian Ocean Tsunami of 2004 and the Tohoko Tsunami of 2011, the possibility of an earthquake  
444 rupture extending up to the seabed was thought to be unlikely. However, clear evidence suggests that the rupture

445 was extended up, nearly to the subduction trench in both cases, and was shallower than what previously thought.  
446 Although the rupture is unlikely to nucleate in shallow depths, it is now widely accepted that deeper events could  
447 extend seaward (Smith et al, 2012). Accordingly, the probabilistic study of tsunami hazards must account for  
448 seabed rupture. Therefore, in addition to the optimistic value of 14-km, we consider 3-km as an alternate updip  
449 rupture depth for buried rupture scenarios. In fact, the 14-km updip rupture depth assumes that the rupture would  
450 not spread into unconsolidated shallow sediments; whereas the 3-km ones takes this into account.

451 We also consider trench faulting as another possible option, suggesting the rupture could extend up to the  
452 seabed. Splay faulting is also considered in this study according to section 2\_7 (for different models of faulting  
453 means buried, splay and trench-breaching see Gao et al., 2018). Thermal and geodetic constraints can help  
454 determine the deep extent of the seismogenic zone, but expert debates are generally determining the shallow extent  
455 extent (e.g. Stirling et al, 2012 for Hikurangi subduction interface).

456

## 457 **2-7 Splay faulting**

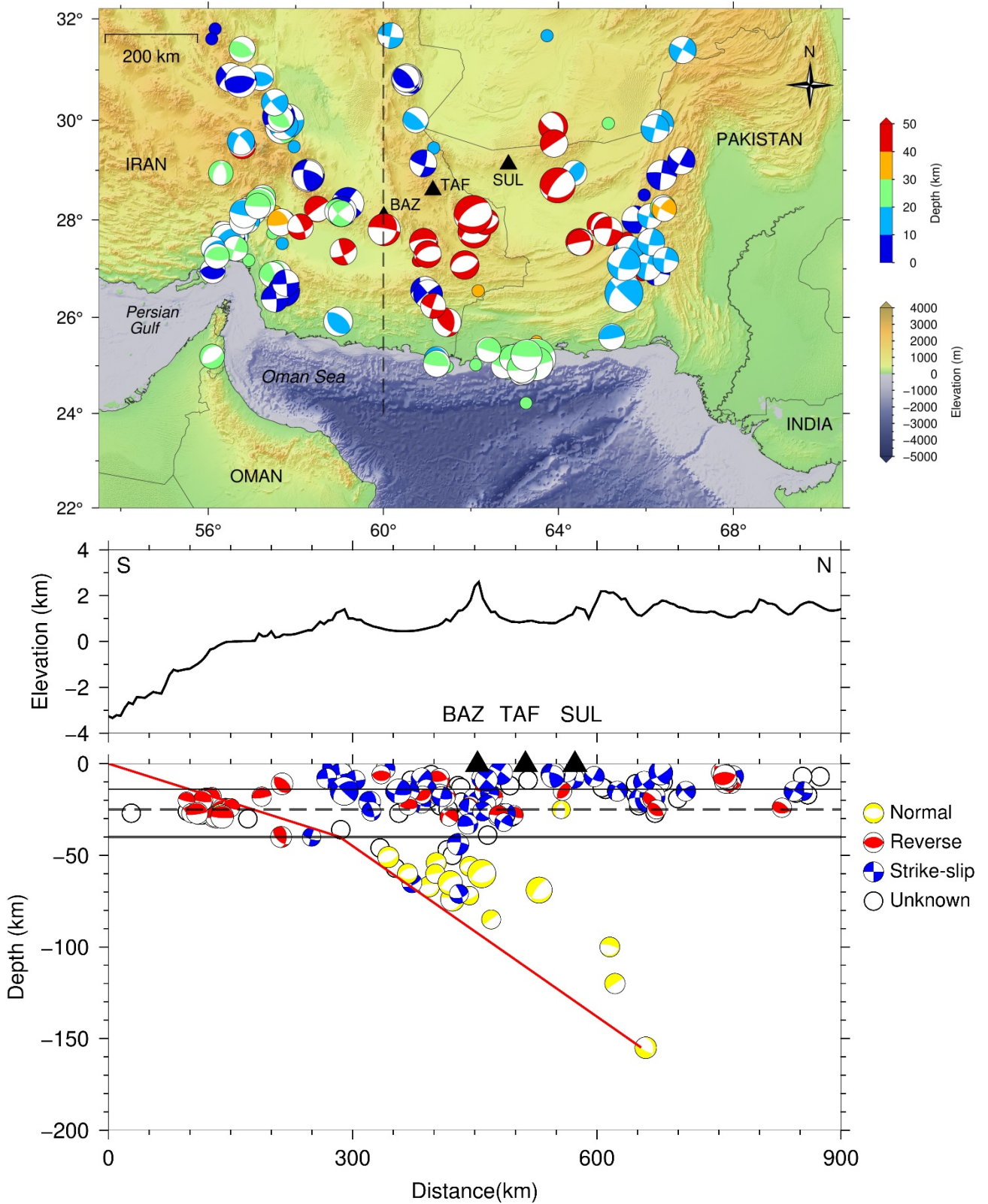
458 Splay faults are secondary faults rising from the plate interface and extend up to the seafloor. They are usually  
459 detected in seismic reflection profiles and exist in many of the subduction zones, including Makran (Grando and  
460 McClay 2007; Smith et al. 2012; Mokhtari 2015). Splay faults can slip during large subducting events or  
461 independently produce earthquakes. They are usually shallow (or even reach the surface) and steeper than the  
462 megathrust and can locally and significantly displace the seafloor and therefore the initial water surface.  
463 Subsequently, they can have a substantial contribution in tsunami hazard at local scale. The 1946 Nankai tsunami  
464 is a good exemplar of splay fault tsunamis (Cummins and Kaneda 2000). The effect of splay faulting in enhancing  
465 the 1960 Chile, 1964 Alaska and 2004 Indian Ocean tsunamis has been also reported (e.g. Plafker 1972; Sibuet et  
466 al. 2007). Splay faulting was brought up as a secondary tsunami source that increased the run-up caused by the  
467 1945 Makran tsunami (Heidarzadeh et al. 2009). The dip of a splay fault can be landward or seaward in which  
468 they both can enhance tsunami wave amplitudes. However, a seaward dipping fault can generate a stronger  
469 tsunami as the shallower part of the fault is toward the sea.

470 Priest et al. (2010) took into account the effect of splay faulting in evaluating tsunami hazard of local  
471 earthquakes in the Cascadia subduction zone. To do so, they developed a logic-tree and assigned different weights  
472 for their scenarios, including splay faulting. In the case of splay fault scenario, the slip is partitioned between the  
473 megathrust and splay fault. Priest et al. (2010) showed that the splay faulting amplifies the tsunami wave height  
474 between 6 to 31% and the run-up between 2 to 20%. The results of tsunami numerical simulation for different  
475 models of faulting (buried, splay and trench-breaching) in Northernmost Cascadia (Gao et al. 2018) shows that  
476 the splay faulting model generate higher tsunami waves (50 to 100%) than the commonly-used model of buried  
477 rupture. Heidarzadeh et al. (2009) studied the effect of splay faulting on tsunami amplitudes in Makran. Their  
478 outcome for a combined tsunami source of the eastern Makran segment and a splay fault indicates the increase of  
479 seabed displacement by 1.5 times and tsunami amplitude by 2 times at some locations.

480 In this study, we incorporate the effect of splay faulting into the tsunami hazard along the coastline of Iran.  
481 We consider a landward splay fault dip of  $35^\circ$  that connects to the megathrust (main fault) at a depth of about 14  
482 km (Fig. 4). We partition the seismic moment of the rupture between the main fault and the splay fault in which  
483 the splay faulting portion ranges from 10% for the largest scenarios to 32% in the case of smallest scenarios.

484

485



486  
487  
488  
489  
490  
491  
492  
493  
494

**Fig. 3** Top: Focal mechanism and depth distribution of Makran seismicity. Bottom: Section of Makran seismicity, based on catalogs with more reliable depths including, normal faults, reverse faults, strike-slip faults, and without mechanism. A line is drawn with a dip angle of 8 degrees from latitude 24 degrees north, which indicates the boundary of the oceanic lithosphere of the sinking Arabian plate below Eurasia. Depths of 14 and 40 km are marked by two continuous horizontal lines. The ratio of vertical scale to horizontal scale is 1 to 3. The triangles show the volcanoes of Bazhman, Taftan, and Sultan in both figures

495 **2-8 Fault rupture locations and slip distributions**

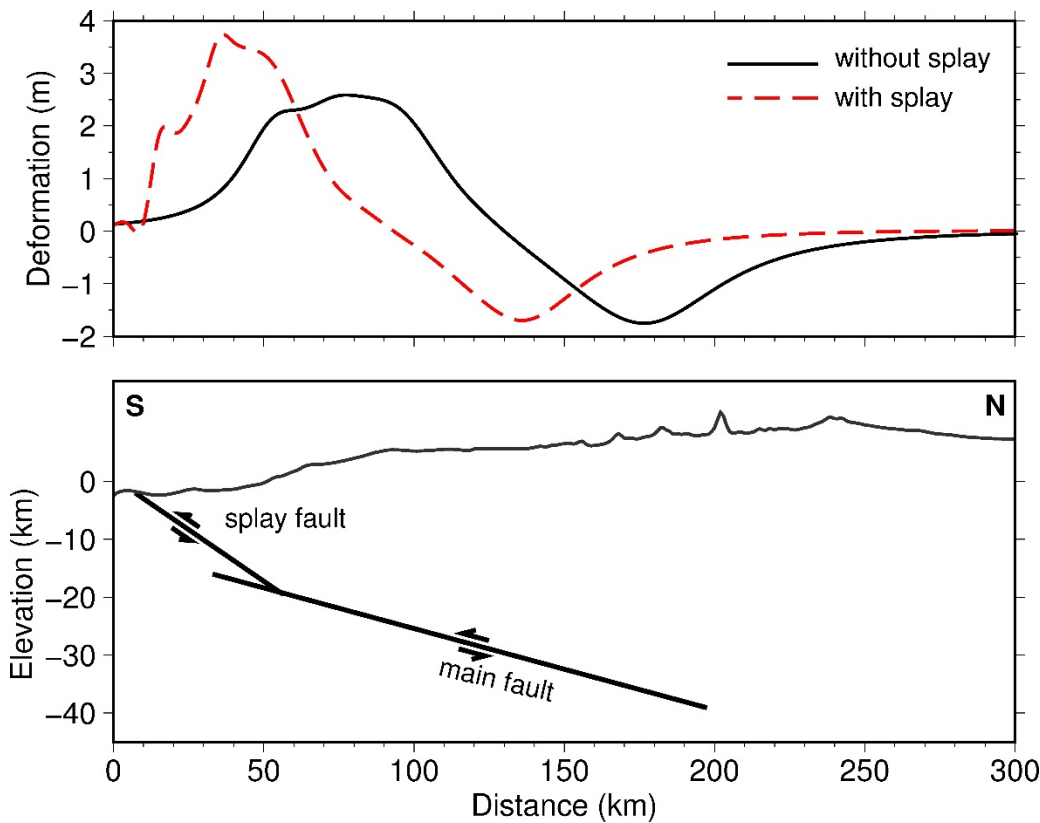
496 Since the occurrence of an earthquake with different magnitudes, in any parts of the MSZ is possible, different  
497 fault locations along the subduction interface should be considered to cover the entire seismic zone. In this way,  
498 more than 155 fault locations which completely cover the MSZ are assumed in this study (Fig. 5).

499 Previous studies (Goda et al. 2014; Ruiz et al. 2015; Sun et al. 2018; e.g. Crempien et al. 2020; Momeni et al.  
500 2020) have shown the amplifying effect of heterogeneous slip distribution on the generated tsunami wave height.  
501 In order to model the heterogeneous slip on the fault, the finite fault technique (Galovič and Brokešová 2004) has  
502 been used in this study. The number of subfaults along the length and dip directions is adjusted based on the  
503 average subfault size of ~15 km ( $\pm 5$  km).

504 The lengths and widths of the rupture plane for each earthquake scenario and the mean and maximum slip  
505 values are calculated using appropriate empirical scaling relationships (Allen and Hayes 2017).

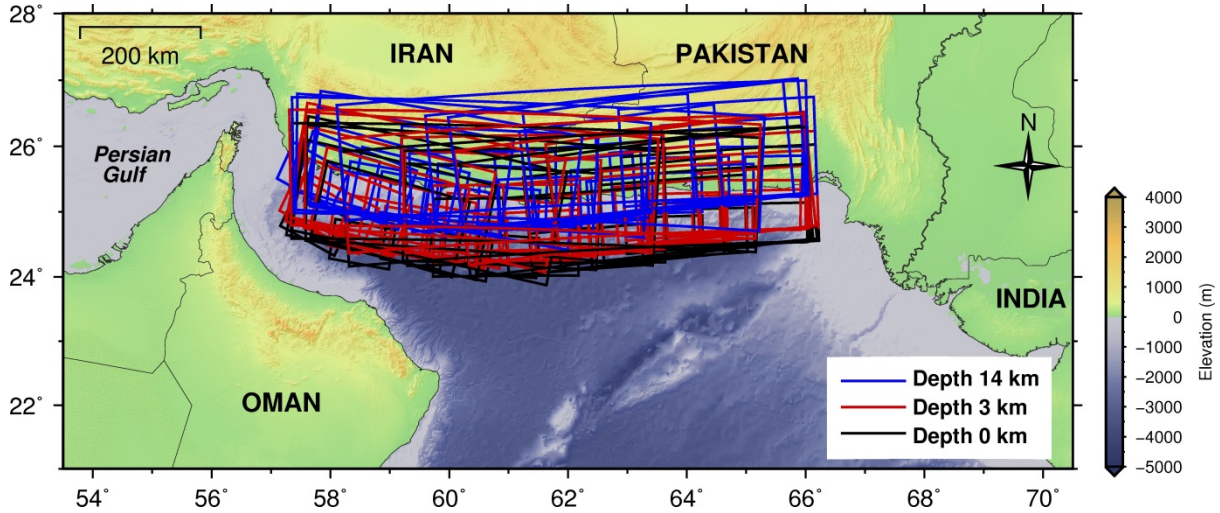
506 To consider aleatory uncertainty of slip distribution, for each fault location, 12 heterogeneous slip scenarios  
507 are generated using k-2 kinematic source modelling (Galovič and Brokešová 2004). The Heterogeneous slip  
508 scenarios are generated considering limitations of average and maximum slipping on fault which are calculated  
509 using Allen and Hayes (2017) scaling relationships. Also taking into account the previous inversion based  
510 earthquake rupture models of interface events (Mai and Thingbaijam 2014), in generating heterogeneous slip  
511 scenarios, placement of slip asperities in the upper one third of the fault in more than 3 of 12 scenarios are not  
512 allowed. In other words, in most of scenarios, slip asperities are located at the deeper parts of the fault. Fig. 6  
513 shows six samples of generated slip distribution scenarios in this study corresponding to Mw 8.0, Mw 8.4, and  
514 Mw 9.0.

515  
516



517  
518 **Fig. 4** Comparison of the seabed displacement in two scenarios with and without splay fault, symbolic representation of  
519 splay fault geometry modeled in Makran seismic hazard simulation

520



521

522

Fig. 5 Considered fault locations in this study which completely cover the MSZ

523

### 3 Probabilistic tsunami hazard analysis (PTHA)

525

526

527

528

529

530

531

532

533

534

535

Due to the uncertainties of the seismic magnitude, fault location, slip distribution, seismicity depth, and splay fault we have considered a number of scenarios according to Table 2 and have performed numerical simulation for each one (section 3-1).

Based on the results of these simulations, for each magnitude  $m$  and each wave height  $z_0$ , the probability of the wave height exceeding a given value of  $z_0$ ,  $P(Z > z_0|m)$  can be obtained. This probability is obtained by integration over the aleatory uncertainties representing the natural uncertainty in the expected wave amplitudes given a specific magnitude of tsunamigenic earthquake.

Hazard curves are obtained for different branches of logic-tree representing epistemic uncertainty.

For each branch of the logic tree, the annual exceedance rate  $v(z_0)$  is calculated based on the following equation:

$$v(z_0) = \sum_{m=M_{min}}^{M_{max}} \lambda(m)P(Z > z_0|m) \quad (5)$$

536

537

538

Where  $\lambda(m)$  is the annual frequency of earthquakes with magnitudes  $m \pm \Delta m/2$ . The magnitude bin size  $\Delta m$  is set as 0.2 magnitude units (see Table 3).

539

540

541

542

543

In the logic tree branches where the activities of the eastern and western zones of Makran are considered different, the random slip distributions, related seabed deformations, and resulting tsunamis for each zone are simulated separately during calculation of the exceedance rate. For these branches, the exceedance rate  $v(z_0)$  is calculated based on the following:

$$v(z_0) = \sum_{n=1}^{N_{Segments}} \sum_{m=M_{min}}^{M_{max}} \lambda_n(m)P(Z > z_0|m) \quad (6)$$

544

545

546

Where  $N_{Segments}$  is equal to 2 (eastern and western MSZs) and  $\lambda_n(m)$  is the annual frequency of earthquakes on source  $n$  with magnitudes between  $m \pm \Delta m/2$ .

547

548

549

The calculation of  $P(Z > z_0|m)$  can be done in two ways. The first method is to form a set of simulated wave heights at the desired point, which are obtained by considering all scenarios within the magnitude bin  $m \pm \Delta m/2$ . Then a wave height like  $z_0$  is selected and the number of wave heights that are greater than  $z_0$  is counted in the

550 set. The ratio of the number of scenarios with wave heights greater than  $z_0$  to the total number of the scenarios  
 551 provides the intended probability at the desired point, which is called here as the real probability.

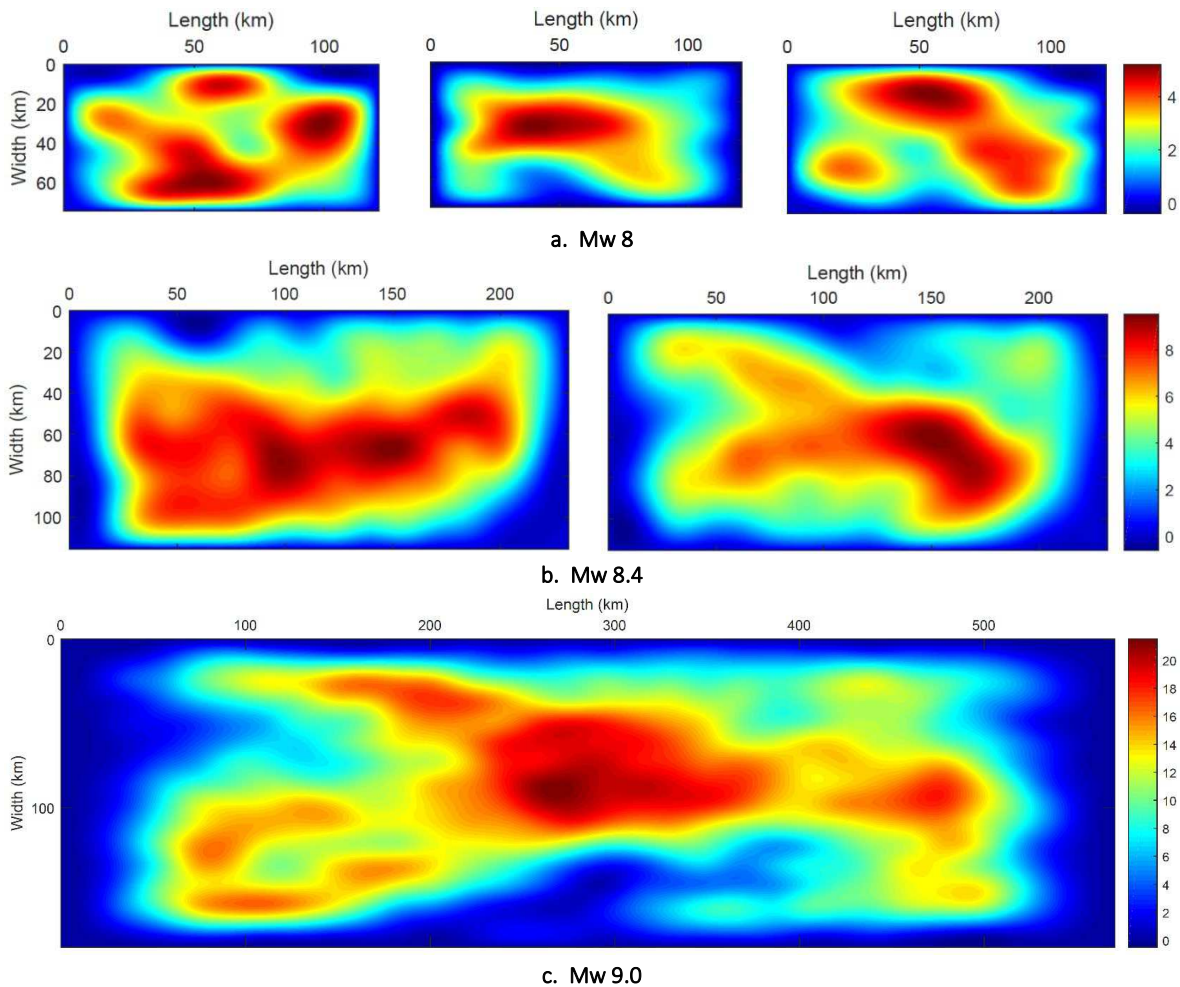
552 In the second method, it is assumed that the desired probability follows the log-normal distribution (e.g.  
 553 Kulkarni et al., 2016). Therefore, by calculating the mean and standard deviation of the set of simulated wave-  
 554 heights, the log-normal distribution is fitted to them.

555 Fig. 7 shows the comparison of the real probability distribution and log-normal distribution in calculating  $P$   
 556 ( $Z > z_0 \mid m$ ), which is presented according to the simulation results for a point on the coast of Chabahar and shows  
 557 that two approaches give similar results, at least for probabilities higher than 0.05.

558 Then based on the assumptions of the logic tree, we calculated the probabilistic tsunami hazard curves for all  
 559 of its branches and formed the statistical population for different hypotheses of the exceedance rate. Based on the  
 560 formed sample population, for each wave height, we calculated exceedance rate at the average, 16%, 50% and  
 561 84% percentiles of distribution.

562 Fig. 8 shows an example of these calculations for a point located on the coast of Chabahar. By reading the  
 563 wave height in the values of 1/475 and 1/2475 from the output hazard curve, it is possible to calculate the value  
 564 of the wave height in the 475-year and 2475-year return periods, at different levels of confidence. It is worth  
 565 noting that a group of hazard curves relating to the eastern Makran scenarios are located below others in Fig. 8.  
 566 The reason for the lower hazard is that Chabahar is in the western Makran, whereas all of the source zones in  
 567 those scenarios are located in the eastern Makran, therefore, the source-receiver distance is comparatively longer  
 568 for this group.

569  
 570



571 Fig. 6 Six examples of generated slip distribution scenarios in this study a. Mw 8.0, b. Mw 8.4, and c Mw 9.0

572 **Table 2.** Number of numerically simulated scenarios due to different fault locations, rupture depth/geometry, and fault slip  
 573 distribution uncertainties. It is notable that item "number of fault depth / geometry scenarios" includes splay faults too.

Seismic magnitude	Number of fault locations	Number of fault depth / geometry scenarios	Number of slip distribution scenarios	Total
7.7-7.9	10	4	12	480
7.9-8.1	7	4	12	336
8.1-8.3	6	4	12	288
8.3-8.5	5	4	12	240
8.5-8.7	4	4	12	196
8.7-8.9	3	4	12	144
8.9-9.1	2	4	12	96
9.1-9.3	2	4	12	96
<b>Total</b>				<b>1872</b>

574

575 **3-1- Tsunami numerical modelling**

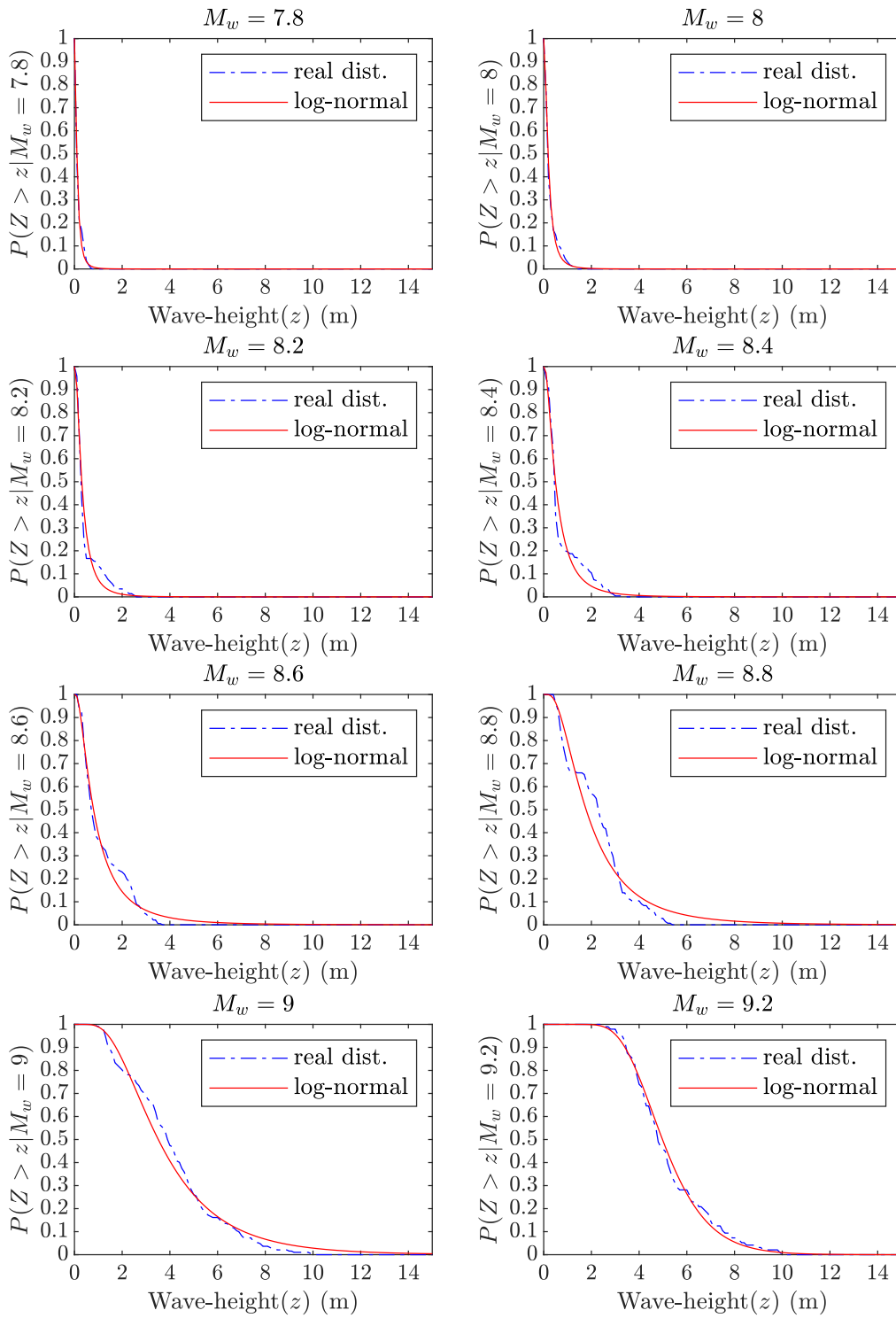
576 The tsunami phenomenon consists of three main phases: generation, propagation, and inundation. Underwater  
 577 earthquakes are the main cause of about 80% of tsunamis (Løvholt 2017). Therefore, we consider only these kind  
 578 of earthquakes as tsunami sources.

579 If the total rupture time of an earthquake is much shorter than the period of the tsunami wave, the seabed  
 580 displacement is considered as an instantaneous motion. This method is conventionally called passive seismic  
 581 generation (Dutykh et al. 2006; Kervella et al. 2007). By using this method, static (rather than dynamic)  
 582 displacement is considered for the seabed due to earthquake. It is also assumed that the initial amplitude of the  
 583 tsunami wave is exactly the same as the amount of vertical displacement of the seabed, because the water of this  
 584 vast area affected by fault sliding cannot be drained within the rupture time (Steketee 1958). Therefore, the initial  
 585 conditions for the propagation of tsunami waves are obtained by transferring the final vertical static displacement  
 586 of the seabed to the water surface. Okada's (1992) closed form solution is used to obtain vertical displacement in  
 587 the seabed. According to this solution, in a semi-infinite homogeneous environment, if the fault is rectangular and  
 588 the amount and direction of slip are constant everywhere on the fault, a closed form solution can be written to  
 589 obtain displacement anywhere in the space. For the faults with non-constant slip, the fault is divided into a number  
 590 of sub-faults, that can be treated separately and the final displacement of the seabed is equal to the sum of all sub-  
 591 fault displacements based on the superposition principle.

592 The source rupture modeling parameters used in this study are listed in Table 3. After tsunami waves are  
 593 generated, they propagate through the water. The most common equations to describe the propagation of tsunami  
 594 waves are the shallow water equations, which are derived from mass and momentum continuity. These equations  
 595 assume that the horizontal scale (wavelength) is much larger than the vertical scale (water depth). The second  
 596 assumption for these equations is that the viscous effect is ignored. As a result of these two assumptions, the  
 597 horizontal velocity of the waves will be much higher than the vertical velocity of the waves, the horizontal velocity  
 598 of the wave will be constant at depth and the pressure will be hydrostatic.

599 This study adopts COMCOT (Cornell Multi-grid COupled Tsunami Model; Liu et al., 1998) as the kernel to  
 600 perform tsunami modeling. COMCOT supports both linear/nonlinear shallow water equations for tsunami  
 601 simulations with the two-grid nesting scheme for flexible computational grid sizes and time steps crossing  
 602 multiple layers and moving boundary scheme for calculating coastal inundation areas and flood depths. On the  
 603 one hand, in deep-water regions where the nonlinear effect is ignored, the linear shallow water equations are used  
 604 for simulating a proposed tsunami from its original source to nearshore regions. On the other hand, in shallow-  
 605 water regions where tsunami waves are amplified by the shoaling effect and bathymetry effect (see, e.g., Imamura  
 606 et al., 1998; Kajiura & Suto, 1990), the nonlinear equations are adopted for calculating nearshore tsunamis. It is  
 607 noted here that both linear and nonlinear shallow water equations are conducted in the spherical coordinate.

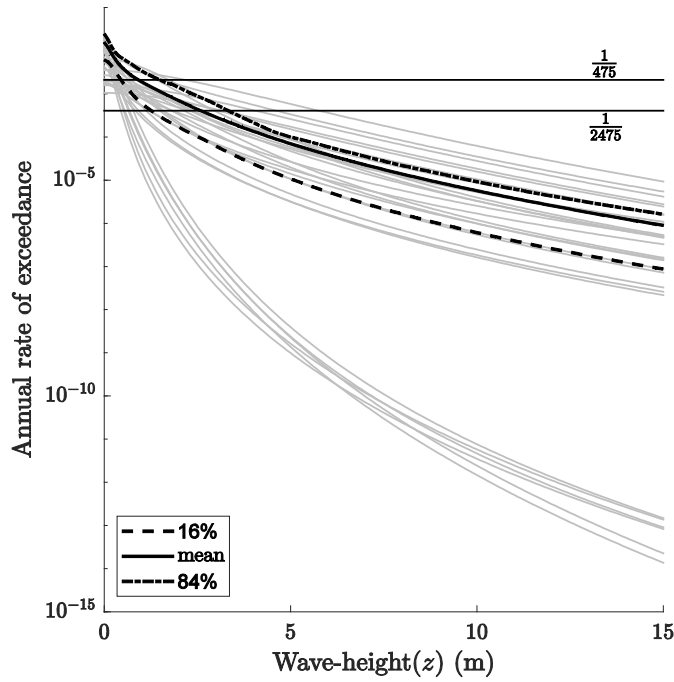
608 As the wavelength of tsunami waves changes due to the water depth, the grid sizes and time steps shall be  
 609 modified accordingly. Thus, we consider the three-layer nested-grid configuration to simulate tsunami waves  
 610 propagating from offshore to nearshore (see Fig. 9).



611

612

Fig. 7 Comparison of real distribution and log-normal for a point on the coast of Chabahar



613  
 614 **Fig. 8** An example of calculating exceedance rate at the 16%, 50% and 84% levels of distribution for a point located on the  
 615 coast of Chabahar, for the 475 and 2475 years return period. Note that a group of hazard curves relating to the eastern  
 616 Makran scenarios are stacked below the others  
 617

618 The grid sizes of the first, second, and third layers are 30, 15, and 5 arc-seconds, respectively. The bathymetry  
 619 data for the first and second layers comes from the General Bathymetric Charts of the Oceans (GEBCO) 2020  
 620 digital grid atlas (IOC, 2003; Weatherall et al., 2015), which has the spatial resolution of 15 arc-seconds. The data  
 621 used in the third layer comes from local data in the Chabahar area with a high spatial resolution of 3 arc-seconds.  
 622 It should be mentioned that we use the Manning's coefficient equal to 0.025 as a standard value for coastal water  
 623 nearshore bottom friction in layer 2 and 3. The computational settings of the nested-grid configuration can be  
 624 found in Table 4.

625 The calculation of the water amplitudes at the shoreline using low-resolution bathymetry data may  
 626 underestimate the tsunami impact (Kamigaichi 2009, 2015).

627 Since in most of the coastal areas of western Makran (except the Chabahar Bay) bathymetry data are only  
 628 available with a maximum resolution of 15 seconds, the Green's law is applied in this study, ensuring the  
 629 calculated shoreline results would not be less than the actual expected values. According to the Green's law  
 630 (conservation of energy), the tsunami wave height farther from the shore is used to approximate the tsunami wave  
 631 height on the shore according to equation (7).

$$h_0 = \sqrt[4]{\frac{d_1}{d_0}} h_1 \quad (7)$$

632  
 633 h and d denote the tsunami wave height and see depth, and indices '0' and '1', respectively, represent the value  
 634 on the shoreline and offshore point.

635 In this study, the height of water on the shoreline is calculated by converted values from a depth of 50 and a  
 636 depth of 10 m. The final result for coastal line is presented using these two values with reasonable weights.

637  
 638  
 639

640

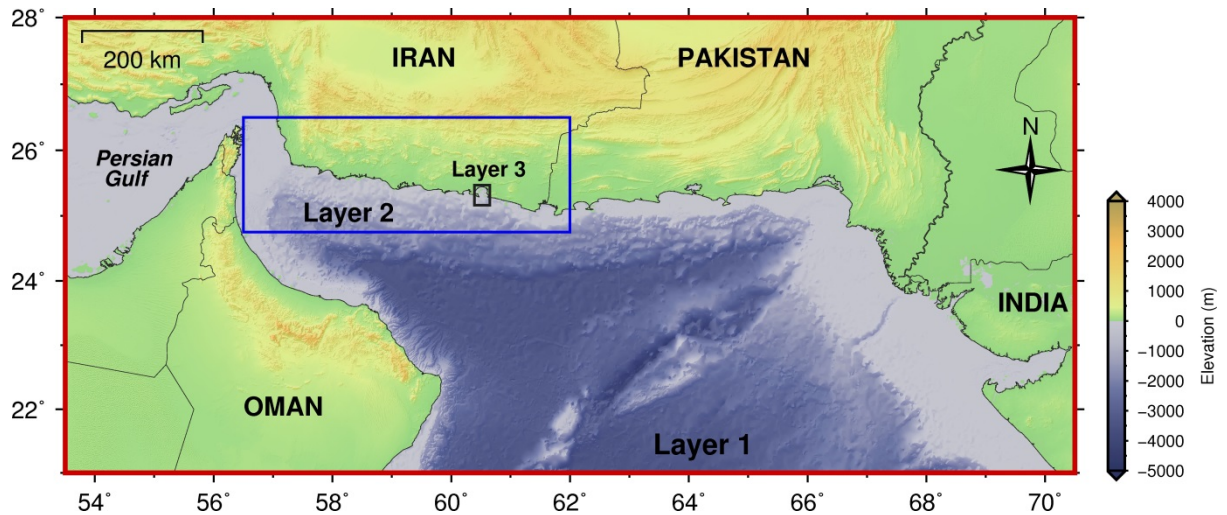
**Table 3.** The source rupture modeling parameters used in this study

Parameter	Values/Ranges
Magnitude (Mw)	7.8 ~ 9.2
Dip angle (degree)	8 (for the main fault) 55 (for splay faults)
Rake angle	90°
Length	65 - 790 (km)
Width	50 - 195 (km)
Average slip	0.8 - 10.5 (m)
Maximum slip	2.4 - 39 (m)
Slip distribution	Heterogeneous
Strike direction	260 - 330
Fault depth (Top of fault)	0, 3 & 14 (km)

641

642

643



644

645

646

647

648

649

650

651

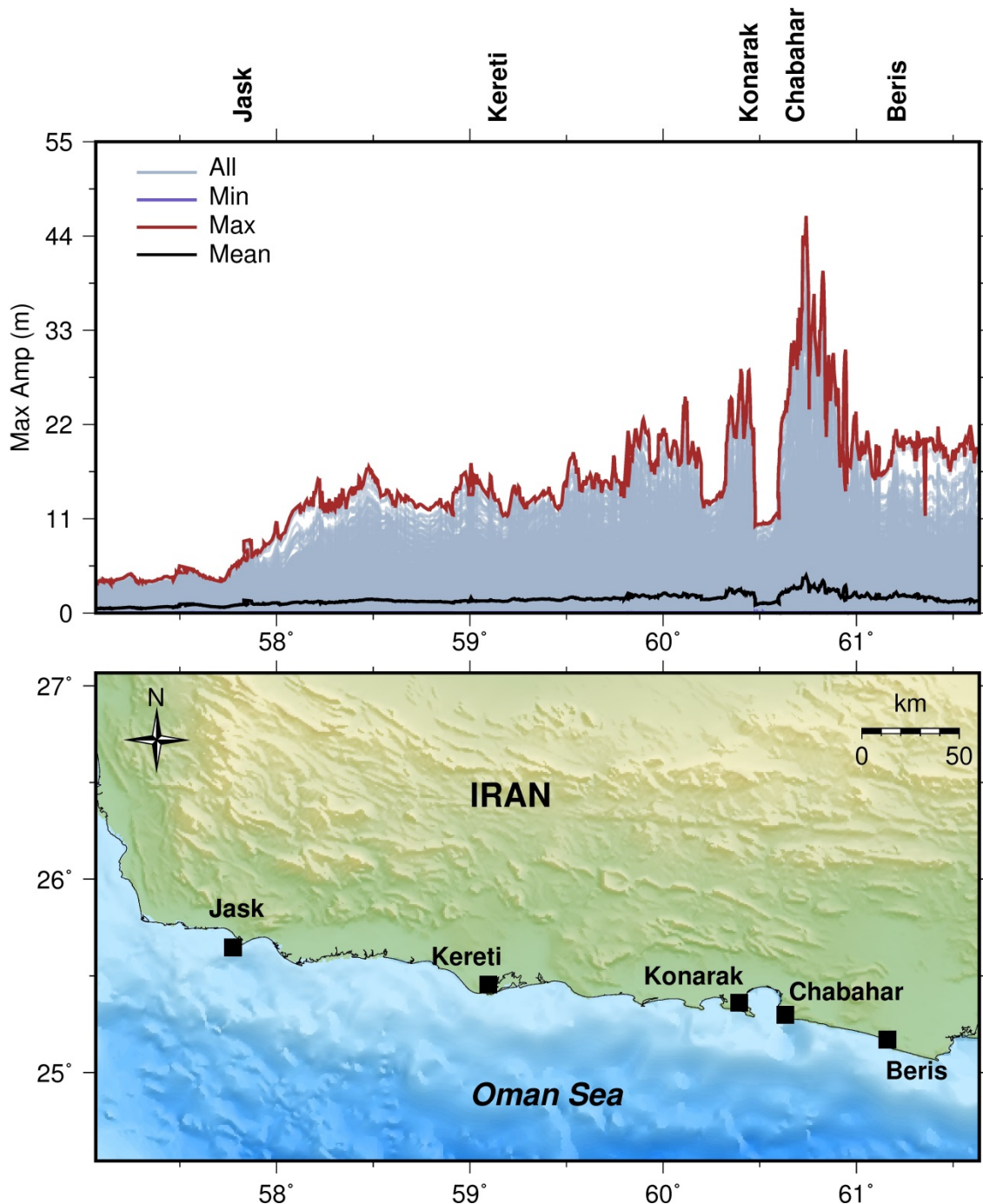
**Fig. 9** Nested grid with three layers used in this study. Layer 1, 30-second grid size (large Rectangle); Layer 2, 15-second grid size (medium Rectangle); and Layer 3, 5-second grid size (small Rectangle)

**Table 4.** The bathymetry data, the grid sizes, the time steps, and the type of equations for three layers used in this study

Layer number	Bathymetry data	grid size ( $\Delta x$ and $\Delta y$ )	Time step	Manning's coefficient	Governing Equations
1	Gebco_15 sec_2020	30 sec	12	-	Linear SWE
2	Gebco_15 sec_2020	15 sec	12	0.025	Nonlinear SWE
3	Local data_3 sec	5 sec	12	0.025	Nonlinear SWE

652

653



654  
655 **Fig. 10** Maximum water height calculated on the shoreline using the modeling results of the 1872 scenarios

656 A number of limit scenarios were considered to select the time required to simulate. The modeling results  
657 show that the maximum amplitude of seismic waves for all stations occurs before the first 6 hours and the  
658 simulation time of 6 hours is a good choice.

659 The results of all numerical modeling (1872 scenarios) are shown in Fig. 10. After completing the numerical  
660 simulations, the PTHA calculation is done according to section 3.

661  
662 **3-2- Earth subsidence**

663 Where the seismic source is a local subduction event (as is possible in the MSZ), in addition to the uplift of  
664 the sea floor, it can cause land subsidence in areas near the coast or on the coast (ASCE7, 2016, Ruiz et al., 2015).  
665 To take into account this effect, the change in the ground elevation per point source is calculated using the Okada

666 (1992) method and the superposition principle is employed for extended fault ruptures. The subsidence is added to  
667 the tsunami wave height on the shore and at the shoreline to retrieve the final results (ASCE7, 2016).

668 In this article, in order to have more realistic assessment of the tsunami water height relative to the reference  
669 ground level, we perform probabilistic hazard calculations once for the height of water from the water free surface  
670 and once for the earth subsidence, and sum up the results of the two, conservatively. Actually this is somehow  
671 conservative, as we know that two maximums do not occur simultaneously.

672 In each modeling, if there was an uplift at any point along the shoreline instead of subsidence, the subsidence  
673 value was considered zero. The results of earth subsidence for western Makran coast, in the vicinity of Sistan va  
674 Baluchestan and Hormozgan provinces, have been calculated in two return periods of 475 and 2475 years with  
675 two levels of average confidence and eighty-four percent (Fig. 13 and Fig. 14).

676 According to this calculation, the maximum subsidence of the coastline with average level of confidence is  
677 0.15 m and 1 m for return periods of 475 and 2475 years, respectively.

678 Moreover, the maximum subsidence of the coastline with 84% level of confidence is 0.5 m and 1.23 m for return  
679 periods of 475 and 2475 years, respectively.

680

#### 681 **4- Results and discussion**

682 In this study, the final results of tsunami wave height for western Makran coast have been calculated in the  
683 form of uniform hazard maps in two return periods of 475 and 2475 years with two confidence levels of mean  
684 and eighty-four percent (Fig. 13 and Fig. 14).

685 The output presented in this study for each 15 km section of the Makran coast is equal to the maximum amount  
686 of probabilistic analysis observed in all points located in that section.

687 Since the return period of 2475 years is more compatible with the long recurrence times of large plate boundary  
688 earthquakes in the MSZ, it is recommended to use the tsunami wave heights of 2475 years (at the mean level) for  
689 structural design purposes. This is consistent with the "maximum considered tsunami" return period adopted  
690 by the ASCE7 (2016) for the United States coastal regions. The more conservative level of 84% could be applied  
691 for critical structures.

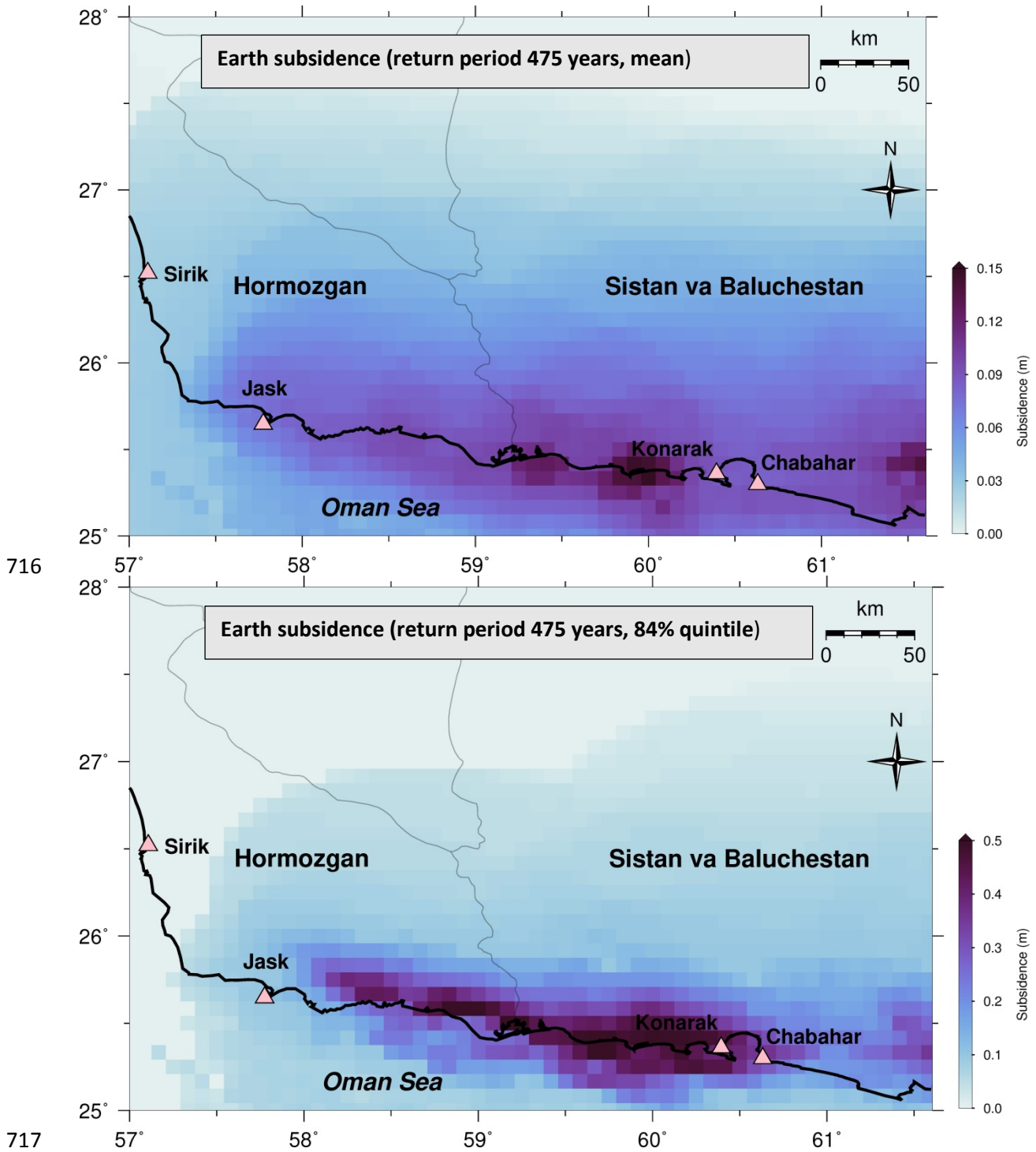
692 Comparison of the output results of our simulations (before applying the probabilistic hazard analysis  
693 algorithm) with simulated scenarios with similar dip angle (8 to 15 degrees) in other places such as the scenarios  
694 of the 1707 Nankai earthquake in Japan (Furumura et al. 2011) and the coast of Sumatra, Indonesia (McCloskey  
695 et al. 2008) indicates the similarity of the range of obtained wave height.

696 Moreover, the accuracy of the probabilistic hazard analysis process is examined and compared with the results for  
697 different coupling coefficients (lower pairing coefficient; lower wave height), different return period (lower return  
698 period; lower wave height) and different confidence levels (lower confidence level; Lower wave height).

699 Finally, it is a good idea to compare the results with some previous regional or global studies, devoted to the  
700 PTHA in the MSZ. In comparisons it should be kept in mind that the subsidence effects are only included in our  
701 results.

702 The probabilistic hazard maps reported by Burbidge et al. (2009) are divided into "high hazard" and "low  
703 hazard" maps based on different assumed maximum magnitudes. They noted that the actual hazard occurs between  
704 these two scenarios. The western segment of the MSZ is not included as a source zone in their low-hazard scenario,  
705 because of the fact that there is no certain knowledge of its potential to produce large tsunamigenic earthquakes.  
706 The highest tsunami amplitudes (in the water depth of 100 m) from these two low and high hazard scenarios along  
707 the coastline of Iran are 0.3 and 2.7 m, Thus, for a return period of 2000 years, applying the Green's Law  
708 approximation (Kamigaichi, 2015), the coastal tsunami amplitudes would be 1.0 and 8.5 m, respectively. In a  
709 more recent study on the PTHA of the Makran region, Hoechner et al. (2016) give tsunami wave heights of 1 and  
710 3 m (for the return period of 500 years) and 4 and 11 m (for the return period of 2500 years), at the Jask and  
711 Chabahar cities that are comparable with our results.

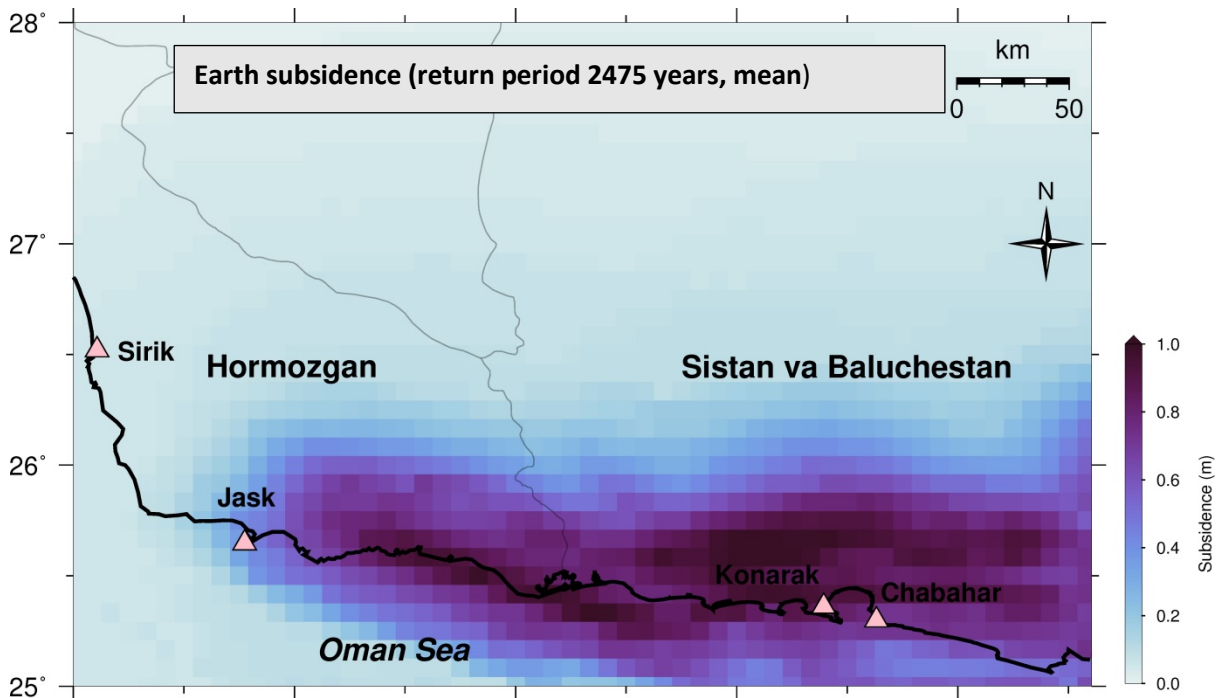
712 Davies et al. (2017) conducted a PTHA on the global scale including the MSZ and showed that the probabilistic  
713 tsunami wave height along the Makran coastlines is generally about the same range, but it decreases towards the  
714 Strait of Hormuz. In their results, tsunami wave amplitude varies between 1.0 to 5.0 m and between 5.0 to 10.0 m  
715 for return periods of 500 and 2500 years, respectively, which is comparable with our results.



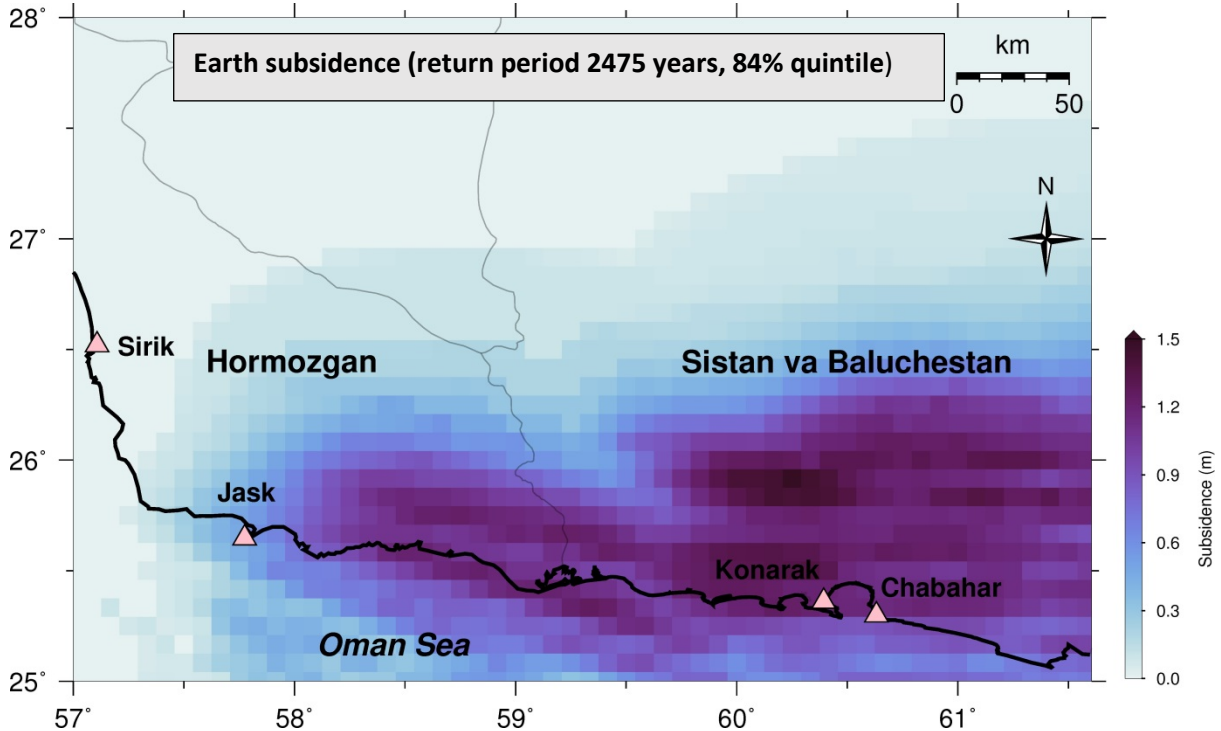
718 **Fig. 11** Earth subsidence plans for western Makran corresponding to a return period of 475 years with two levels of average  
 719 confidence and eighty-four percent

720  
 721  
 722  
 723  
 724  
 725

726  
727



728

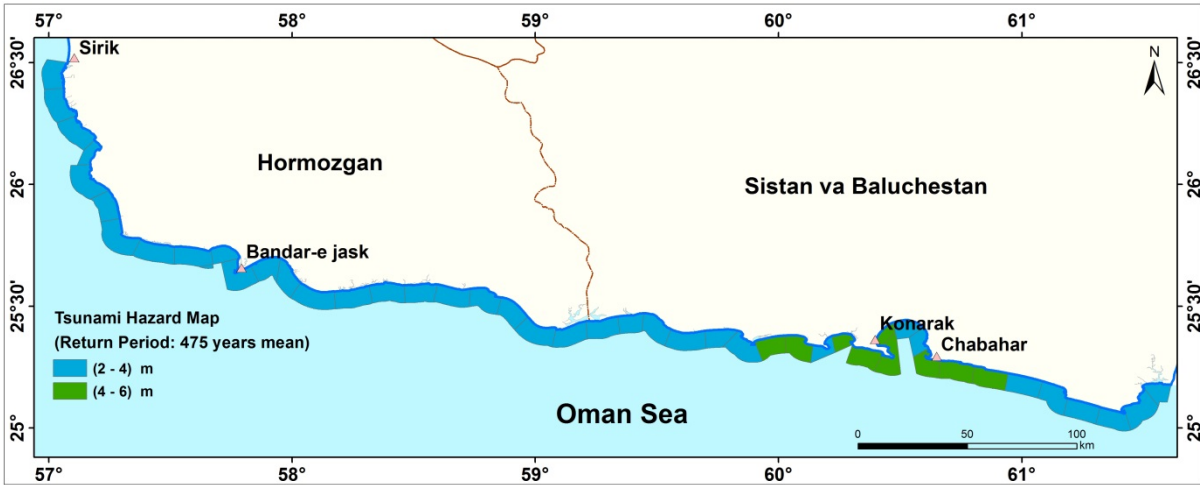
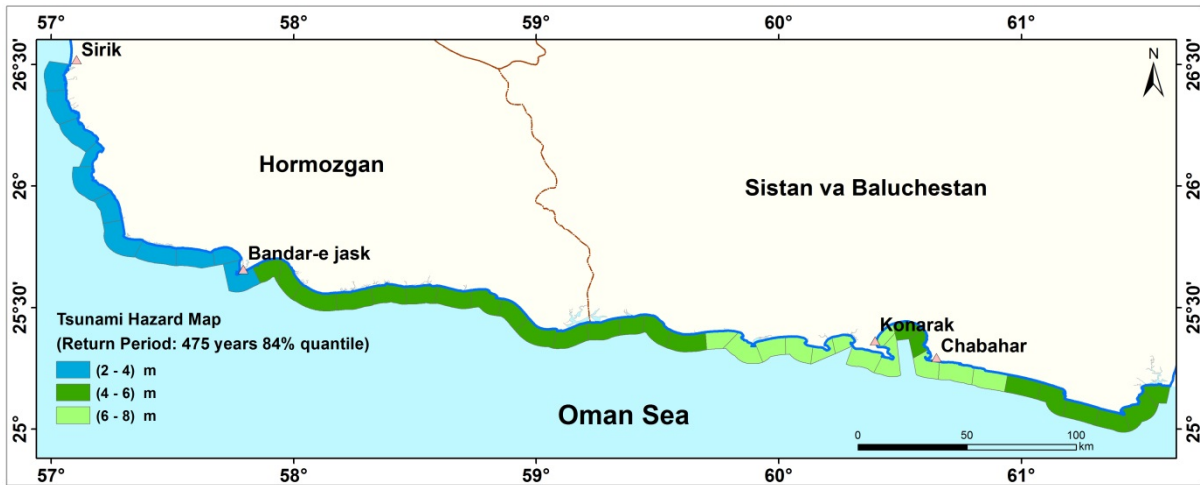


729  
730

731 **Fig. 12** Earth subsidence plans for western Makran corresponding to a return period of 2475 years with two levels of  
732 average confidence and eighty-four percent

733  
734  
735  
736

737  
738



742  
743

Fig. 13 Uniform hazard plans for western Makran corresponding to a return period of 475 years with two confidence levels of mean and eighty-four percent

744

745

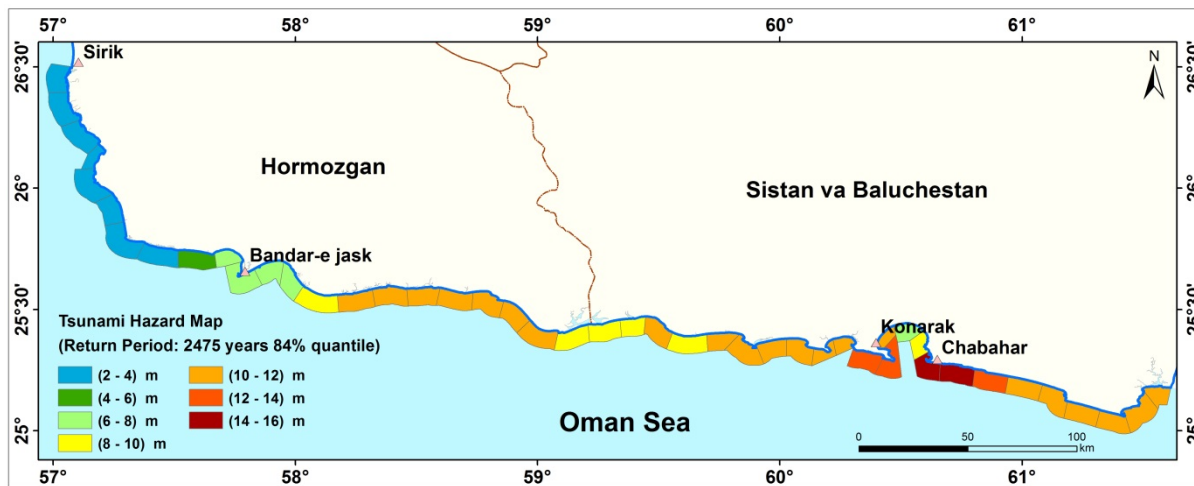
746

747

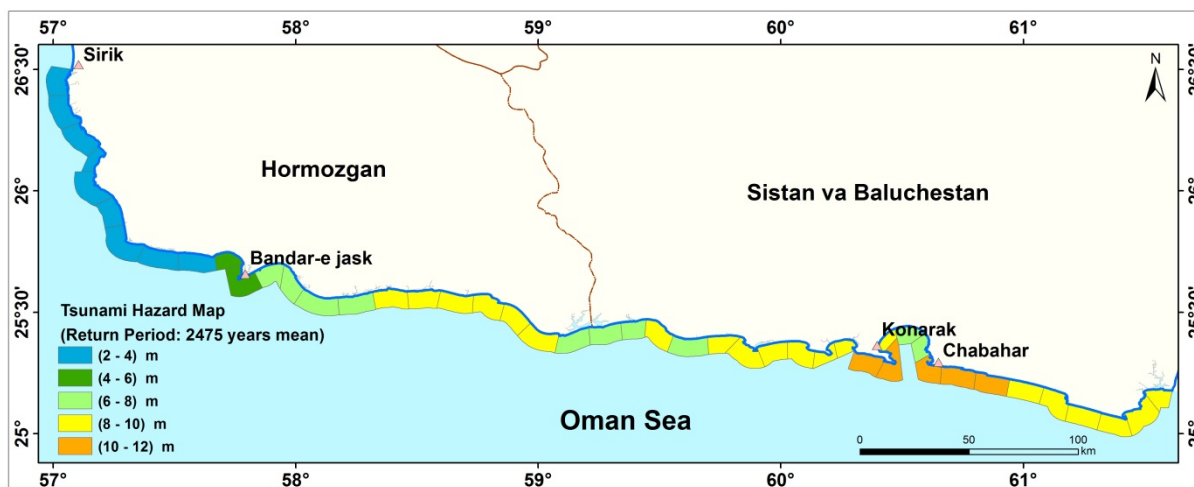
748

749

750



751



752 Fig. 14 Uniform hazard plans for western Makran corresponding to a return period of 2475 years with two confidence  
 753 levels of mean and eighty-four percent

754 **5- Conclusions**

755 This study presents the first tsunami hazard zonation in the coastal area of western Makran using probabilistic  
 756 tsunami hazard assesment, including all possible uncertainties and earth subsidence effects. The results are  
 757 expressed in terms of uniform hazard maps for two return periods of 475 and 2475 years at two confidence  
 758 levels of average and eighty-four percent. As tsunamis generated by far-field tectonic sources cause very little  
 759 effect on this part, we consider only tsunamis of earthquake origin generated in the MSZ.

760 The uncertainty of maximum seismic magnitude, scaling relations, earthquake occurrence model, continuity  
 761 of seismic zone, seismic coupling coefficient, depth of rupture, splay fault, fault locations, and fault slip  
 762 distribution are included in PTHA calculation for this region. We use the COMCOT tsunami modelling code to  
 763 simulate 1872 scenarios.

764 The result shows that Chabahar and Sirik are respectively exposed to the highest and lowest probable water  
 765 heights due to the tsunami.

766 In this study we do our best to have reliable assesment for PTHA in the west MSZ. However, it is important  
 767 to consider its limitations and try to reduce them as possible in future studies. In this study, we consider underwater  
 768 earthquakes as the only sources for tsunami, but it seems appropriate to study the investigate seabed landslides as  
 769 another possible causes of tsunami and their combination with earthquakes in MSZ. In addition, in our study we  
 770 ignore the dynamic interaction between the tides and tsunami waves. Therefore, to use the probabilistic tsunami  
 771 water height presented in this study it is necessary to add the value of corresponding maximum tidal height at any  
 772 location, conservatively. More accurate results can be achieved by considering this dynamic interaction. Finally,

773 we should mention the importance role of high quality bathymetry and topography data for more accurate PTHA  
774 results, especially for simulation of inundation and runup that we hope to consider in our future studies.

775

## 776 **References**

- 777 Abrahamson NA, Bommer JJ (2005) Probability and uncertainty in seismic hazard analysis. *Earthq spectra*  
778 21:603–607
- 779 Aldama-Bustos G, Bommer JJ, Fenton CH, Stafford PJ (2009) Probabilistic seismic hazard analysis for rock  
780 sites in the cities of Abu Dhabi, Dubai and Ra's Al Khaymah, United Arab Emirates. *Georisk* 3:1–29.  
781 <https://doi.org/10.1080/17499510802331363>
- 782 Allen TI, Hayes GP (2017) Alternative rupture-scaling relationships for subduction interface and other offshore  
783 environments. *Bull Seismol Soc Am* 107:1240–1253. <https://doi.org/10.1785/0120160255>
- 784 Ambraseys NN, Melville CP (1982) A history of Persian earthquakes. Cambridge university press
- 785 Anderson JG, Luco JE (1983) Consequences of slip rate constraints on earthquake occurrence relations. *Bull*  
786 *Seismol Soc Am* 73:471–496
- 787 Annaka T, Satake K, Sakakiyama T, et al (2007) Logic-tree approach for Probabilistic Tsunami Hazard  
788 Analysis and its applications to the Japanese coasts. *Pure Appl Geophys* 164:577–592.  
789 <https://doi.org/10.1007/s00024-006-0174-3>
- 790 Atkinson GM, Goda K (2011) Effects of seismicity models and new ground-motion prediction equations on  
791 seismic hazard assessment for four Canadian cities. *Bull Seismol Soc Am* 101:176–189.  
792 <https://doi.org/10.1785/0120100093>
- 793 Bayrak Y, Yilmaztürk A, Öztürk S (2002) Lateral variations of the modal (a/b) values for the different regions  
794 of the world. *J Geodyn* 34:653–666. [https://doi.org/10.1016/S0264-3707\(02\)00037-6](https://doi.org/10.1016/S0264-3707(02)00037-6)
- 795 Benito MB, Lindholm C, Camacho E, et al (2012) A new evaluation of seismic hazard for the Central America  
796 Region. *Bull Seismol Soc Am* 102:504–523. <https://doi.org/10.1785/0120110015>
- 797 Berryman K, Wallace L, Hayes G, et al (2015) The GEM faulted earth subduction interface characterisation  
798 project. GNS Science
- 799 Blaser L, Krüger F, Ohrnberger M, Scherbaum F (2010) Scaling relations of earthquake source parameter  
800 estimates with special focus on subduction environment. *Bull Seismol Soc Am* 100:2914–2926.  
801 <https://doi.org/10.1785/0120100111>
- 802 Burbidge DR, Cummins PR, Mleczko R, et al (2009) A Probabilistic Tsunami Hazard Assessment of the Indian  
803 Ocean Nations. *Geosci Aust Prof Opin* 78–79
- 804 Byrne DE, Sykes LR, Davis DM (1992) Great Thrust Earthquakes and Aseismic Slip Along the Plate Boundary  
805 of the Makran motion in the form of earthquakes may occur in a variety ( e . g . , southern Chile ), while  
806 still others have experienced no of ways at subduction zones . Some margins produ. *J Geophys Res*  
807 97:449–478
- 808 Crempien JGF, Urrutia A, Benavente R, Cienfuegos R (2020) Effects of earthquake spatial slip correlation on  
809 variability of tsunami potential energy and intensities. *Sci Rep* 10:1–10. <https://doi.org/10.1038/s41598-020-65412-3>
- 810 Cummins PR, Kaneda Y (2000) Possible splay fault slip during the 1946 Nankai earthquake
- 811 Davies G, Griffin J, Løvholt F, et al (2017) A global probabilistic tsunami hazard assessment from earthquake  
812 sources. *Geol Soc Spec Publ* 456:219–244. <https://doi.org/10.1144/sp456.5>
- 813 Deif A, El-Hussain I (2012) Seismic moment rate and earthquake mean recurrence interval in the major tectonic  
814 boundaries around Oman. *J Geophys Eng* 9:773–783. <https://doi.org/10.1088/1742-2132/9/6/773>
- 815 Dutykh D, Dias F, Kervella Y (2006) Linear theory of wave generation by a moving bottom. *Comptes Rendus*  
816 *Math* 343:499–504
- 817 El-Hussain I, Omira R, Al-Habsi Z, et al (2018) Probabilistic and deterministic estimates of near-field tsunami  
818 hazards in northeast Oman. *Geosci Lett* 5:. <https://doi.org/10.1186/s40562-018-0129-4>
- 819 El-Hussain I, Omira R, Deif A, et al (2016) Probabilistic tsunami hazard assessment along Oman coast from  
820 submarine earthquakes in the Makran subduction zone. *Arab J Geosci* 9:. <https://doi.org/10.1007/s12517-016-2687-0>
- 821 Frohling E, Szeliga W (2016a) GPS constraints on interplate locking within the Makran subduction zone.  
822 *Geophys J Int* 205:67–76. <https://doi.org/10.1093/gji/ggw001>
- 823 Frohling E, Szeliga W (2016b) GPS constraints on interplate locking within the Makran subduction zone.  
824 *Geophys Suppl to Mon Not R Astron Soc* 205:67–76
- 825 Furumura T, Imai K, Maeda T (2011) A revised tsunami source model for the 1707 Hōei earthquake and  
826 simulation of tsunami inundation of Ryujin Lake, Kyushu, Japan. *J Geophys Res Solid Earth* 116:.  
827 <https://doi.org/10.1029/2010JB007918>
- 828 Gallovič F, Brokešová J (2004) The k-2 Rupture Model Parametric Study: Example of the 1999 Athens  
829 Earthquake. *Stud Geophys Geod* 48:589–613. <https://doi.org/10.1023/B:SGEG.0000037473.70906.08>
- 830
- 831

832 Gao D, Wang K, Insua TL, et al (2018) Defining megathrust tsunami source scenarios for northernmost  
833 Cascadia. *Nat Hazards* 94:445–469. <https://doi.org/10.1007/s11069-018-3397-6>

834 Ghadimi Moghaddam H, Khodaverdian A, Zafarani H Long term fault slip rates, distributed deformation rates  
835 and forecast of seismicity in the Makran Region

836 Goda K, Mai PM, Yasuda T, Mori N (2014) Sensitivity of tsunami wave profiles and inundation simulations to  
837 earthquake slip and fault geometry for the 2011 Tohoku earthquake. *Earth, Planets Sp* 66:1–20.  
838 <https://doi.org/10.1186/1880-5981-66-105>

839 Grando G, McClay K (2007) Morphotectonics domains and structural styles in the Makran accretionary prism,  
840 offshore Iran. *Sediment Geol* 196:157–179. <https://doi.org/10.1016/j.sedgeo.2006.05.030>

841 Hanks TC, Kanamori H (1979) *Eo.* 84:2348–2350

842 Hayes GP, Moore GL, Portner DE, et al (2018) Slab2, a comprehensive subduction zone geometry model

843 Hayes GP, Wald DJ, Johnson RL (2012) Slab1.0: A three-dimensional model of global subduction zone  
844 geometries. *J Geophys Res Solid Earth* 117:1–15. <https://doi.org/10.1029/2011JB008524>

845 Heidarzadeh M, Kijko A (2011) A probabilistic tsunami hazard assessment for the Makran subduction zone at  
846 the northwestern Indian Ocean. *Nat Hazards* 56:577–593. <https://doi.org/10.1007/s11069-010-9574-x>

847 Heidarzadeh M, Pirooz MD, Zaker NH, et al (2008) Historical tsunamis in the Makran Subduction Zone off the  
848 southern coasts of Iran and Pakistan and results of numerical modeling. *Ocean Eng* 35:774–786.  
849 <https://doi.org/10.1016/j.oceaneng.2008.01.017>

850 Heidarzadeh M, Pirooz MD, Zaker NH (2009) Modeling the near-field effects of the worst-case tsunami in the  
851 Makran subduction zone. *Ocean Eng* 36:368–376. <https://doi.org/10.1016/j.oceaneng.2009.01.004>

852 Heuret A, Lallemand S, Funicello F, et al (2011) Physical characteristics of subduction interface type  
853 seismogenic zones revisited. *Geochemistry, Geophys Geosystems* 12:1–26.  
854 <https://doi.org/10.1029/2010GC003230>

855 Hoechner A, Babeyko AY, Zamora N (2016) Probabilistic tsunami hazard assessment for the Makran region  
856 with focus on maximum magnitude assumption. *Nat Hazards Earth Syst Sci* 16:1339–1350.  
857 <https://doi.org/10.5194/nhess-16-1339-2016>

858 Hydro BC (2012) Probabilistic Seismic Hazard Analysis (PSHA) Model, Volumes 1, 2, 3 and 4. BC Hydro

859 IHO (2003) BODC: Centenary Edition of the GEBCO Digital Atlas, published on CD-ROM on behalf of the  
860 Intergovernmental Oceanographic Commission and the International Hydrographic Organization as part  
861 of the General Bathymetric Chart of the Oceans. Br Oceanogr Data Centre, Liverpool, UK 52:

862 Jaiswal RK, Singh AP, Rastogi BK (2009) Simulation of the Arabian Sea Tsunami propagation generated due to  
863 1945 Makran Earthquake and its effect on western parts of Gujarat (India). *Nat Hazards* 48:245–258.  
864 <https://doi.org/10.1007/s11069-008-9261-3>

865 Kagan YY (2002) Seismic moment distribution revisited: II. Moment conservation principle. *Geophys J Int*  
866 149:731–754. <https://doi.org/10.1046/j.1365-246X.2002.01671.x>

867 Kamigaichi O (2009) Tsunami forecasting and warning. In: *Extreme Environmental Events*

868 Kamigaichi O (2015) Tsunami Forecasting and Warning. *Encycl Complex Syst Sci* 1–38.  
869 [https://doi.org/10.1007/978-3-642-27737-5\\_568-3](https://doi.org/10.1007/978-3-642-27737-5_568-3)

870 Kervella Y, Dutykh D, Dias F (2007) Comparison between three-dimensional linear and nonlinear tsunami  
871 generation models. *Theor Comput fluid Dyn* 21:245–269

872 Kopp C, Fruehn J, Flueh ER, et al (2000) Structure of the Makran subduction zone from wide-angle and  
873 reflection seismic data. *Tectonophysics* 329:171–191. [https://doi.org/https://doi.org/10.1016/S0040-1951\(00\)00195-5](https://doi.org/https://doi.org/10.1016/S0040-1951(00)00195-5)

874

875 Kulkarni RB, Youngs RR, Coppersmith KJ (1984) Assessment of confidence intervals for results of seismic  
876 hazard analysis. In: *Proceedings of the eighth world conference on earthquake engineering.* pp 263–270

877 Kulkarni V, Arcos MEM, Alcinov T, et al (2016) Probabilistic tsunami hazard assessment for a site in eastern  
878 Canada. *Pure Appl Geophys* 173:3719–3755

879 Løvholt F (2017) 2 . Tsunami Hazard and Risk Assessment. 1–9

880 Løvholt F, Pedersen G, Bazin S, et al (2012) Stochastic analysis of tsunami runup due to heterogeneous  
881 coseismic slip and dispersion. *J Geophys Res Ocean* 117:1–17. <https://doi.org/10.1029/2011JC007616>

882 Maggi A, Jackson JA, Priestley K, Baker C (2000) A re-assessment of focal depth distributions in southern Iran,  
883 the Tien Shan and northern India: Do earthquakes really occur in the continental mantle? *Geophys J Int*  
884 143:629–661. <https://doi.org/10.1046/j.1365-246X.2000.00254.x>

885 Mai PM, Thingbaijam KKS (2014) SRCMOD: An Online Database of Finite-Fault Rupture Models. *Seismol*  
886 *Res Lett* 85:1348–1357. <https://doi.org/10.1785/0220140077>

887 McAdoo BG, Capone MK, Minder J (2004) Seafloor geomorphology of convergent margins: Implications for  
888 Cascadia seismic hazard. *Tectonics* 23:. <https://doi.org/https://doi.org/10.1029/2003TC001570>

889 McCloskey J, Antonioli A, Piatanesi A, et al (2008) Tsunami threat in the Indian Ocean from a future  
890 megathrust earthquake west of Sumatra. *Earth Planet Sci Lett* 265:61–81.  
891 <https://doi.org/10.1016/j.epsl.2007.09.034>

892 Meletti C, D'Amico V, Martinelli F (2010) Homogeneous determination of maximum magnitude  
893 Mokhtari M (2015) The role of splay faulting in increasing the devastation effect of tsunami hazard in Makran,  
894 Oman Sea. *Arab J Geosci* 8:4291–4298. <https://doi.org/10.1007/s12517-014-1375-1>  
895 Momeni P, Goda K, Heidarzadeh M, Qin J (2020) Stochastic analysis of tsunami hazard of the 1945 Makran  
896 subduction zone MW 8.1–8.3 earthquakes. *Geosci* 10:1–20. <https://doi.org/10.3390/geosciences10110452>  
897 Muldashev IA, Sobolev S V. (2020) What Controls Maximum Magnitudes of Giant Subduction Earthquakes?  
898 *Geochemistry, Geophys Geosystems* 21:. <https://doi.org/10.1029/2020GC009145>  
899 Murotani S, Satake K, Fujii Y (2013) Scaling relations of seismic moment, rupture area, average slip, and  
900 asperity size for M~9 subduction-zone earthquakes. *Geophys Res Lett* 40:5070–5074.  
901 <https://doi.org/10.1002/grl.50976>  
902 Musson RMW (2009) Subduction in the Western Makran: the historian's contribution. *J Geol Soc*  
903 London 166:387 LP – 391. <https://doi.org/10.1144/0016-76492008-119>  
904 Neetu S, Suresh I, Shankar R, et al (2011) Trapped waves of the 27 November 1945 Makran tsunami:  
905 Observations and numerical modeling. *Nat Hazards* 59:1609–1618. [https://doi.org/10.1007/s11069-011-](https://doi.org/10.1007/s11069-011-9854-0)  
906 [9854-0](https://doi.org/10.1007/s11069-011-9854-0)  
907 Okada Y (1992) Internal deformation due to shear and tensile faults in a half-space. *Bull Seismol Soc Am*  
908 82:1018–1040  
909 Pacheco JF, Sykes LR, Scholz CH (1993) Nature of seismic coupling along simple plate boundaries of the  
910 subduction type. *J Geophys Res* 98:. <https://doi.org/10.1029/93jb00349>  
911 Pajang S, Cubas N, Letouzey J, et al (2021) Seismic hazard of the western Makran subduction zone: Insight  
912 from mechanical modelling and inferred frictional properties. *Earth Planet Sci Lett* 562:116789.  
913 <https://doi.org/https://doi.org/10.1016/j.epsl.2021.116789>  
914 Papazachos B, Scordilis E, Panagiotopoulos D, et al (2004) GLOBAL RELATIONS BETWEEN SEISMIC  
915 FAULT PARAMETERS AND MOMENT MAGNITUDE OF EARTHQUAKES. *Bull Geol Soc Greece*  
916 36:1482–1489  
917 Penney C, Tavakoli F, Saadat A, et al (2017) Megathrust and accretionary wedge properties and behaviour in  
918 the Makran subduction zone. *Geophys J Int* 209:1800–1830. <https://doi.org/10.1093/gji/ggx126>  
919 Pisarenko VF, Sornette D (2004) Statistical detection and characterization of a deviation from the Gutenberg-  
920 Richter distribution above magnitude 8. *Pure Appl Geophys* 161:839–864.  
921 <https://doi.org/10.1007/s00024-003-2475-0>  
922 Plafker G (1972) Alaskan earthquake of 1964 and Chilean earthquake of 1960: Implications for arc tectonics. *J*  
923 *Geophys Res* 77:901–925  
924 Power WL (2013) Review of tsunami hazard in New Zealand (2013 update). Ministry of Civil Defence and  
925 Emergency Management  
926 Priest GR, Goldfinger C, Wang K, et al (2010) Confidence levels for tsunami-inundation limits in northern  
927 Oregon inferred from a 10,000-year history of great earthquakes at the Cascadia subduction zone. *Nat*  
928 *Hazards* 54:27–73. <https://doi.org/10.1007/s11069-009-9453-5>  
929 Rashidi A, Zafarani H, Tatar M (2020a) Geometric characteristics of the Makran's subduction zone. *Tectonics*  
930 12:  
931 Rashidi A, Zaher , Shomali H, et al (2020b) Tsunami hazard assessment in the Makran subduction zone.  
932 100:861–875. <https://doi.org/10.1007/s11069-019-03848-1>  
933 Ruff L, Kanamori H (1980) Seismicity and the subduction process. *Phys Earth Planet Inter* 23:240–252.  
934 [https://doi.org/https://doi.org/10.1016/0031-9201\(80\)90117-X](https://doi.org/https://doi.org/10.1016/0031-9201(80)90117-X)  
935 Ruiz JA, Fuentes M, Riquelme S, et al (2015) Numerical simulation of tsunami runup in northern Chile based  
936 on non-uniform k–2 slip distributions. *Nat Hazards* 79:1177–1198. [https://doi.org/10.1007/s11069-015-](https://doi.org/10.1007/s11069-015-1901-9)  
937 [1901-9](https://doi.org/10.1007/s11069-015-1901-9)  
938 Scholz CH, Campos J (2012) The seismic coupling of subduction zones revisited. *J Geophys Res Solid Earth*  
939 117:1–22. <https://doi.org/10.1029/2011JB009003>  
940 Schwartz SY (1999) Noncharacteristic behavior and complex recurrence of large subduction zone earthquakes. *J*  
941 *Geophys Res Solid Earth* 104:23111–23125. <https://doi.org/10.1029/1999jb900226>  
942 Sibuet J-C, Rangin C, Le Pichon X, et al (2007) 26th December 2004 great Sumatra–Andaman earthquake: Co-  
943 seismic and post-seismic motions in northern Sumatra. *Earth Planet Sci Lett* 263:88–103  
944 Skarlatoudis AA, Somerville PG, Thio HK (2016) Source-scaling relations of interface subduction earthquakes  
945 for strong ground motion and tsunami simulation. *Bull Seismol Soc Am* 106:1652–1662.  
946 <https://doi.org/10.1785/0120150320>  
947 Smith G, McNeill L, Henstock IJ, Bull J (2012) The structure and fault activity of the Makran accretionary  
948 prism. *J Geophys Res Solid Earth* 117:1–17. <https://doi.org/10.1029/2012JB009312>  
949 Steketee JA (1958) ON VOLTERRA'S DISLOCATIONS IN A SEMI-INFINITE ELASTIC MEDIUM. *Can J*  
950 *Phys* 36:192–205. <https://doi.org/10.1139/p58-024>  
951 Stewart JP, Chiou S-J, Bray JD, et al (2002) Ground motion evaluation procedures for performance-based

952 design. *Soil Dyn Earthq Eng* 22:765–772. [https://doi.org/https://doi.org/10.1016/S0267-7261\(02\)00097-0](https://doi.org/https://doi.org/10.1016/S0267-7261(02)00097-0)  
953 Strasser FO, Arango MC, Bommer JJ (2010) Scaling of the Source Dimensions of Interface and Intraslab  
954 Subduction-zone Earthquakes with Moment Magnitude. *Seismol Res Lett* 81:941–950.  
955 <https://doi.org/10.1785/gssrl.81.6.941>  
956 Sun Y-S, Chen P-F, Chen C-C, et al (2018) Assessment of the peak tsunami amplitude associated with a large  
957 earthquake occurring along the southernmost Ryukyu subduction zone in the region of Taiwan. *Nat*  
958 *Hazards Earth Syst Sci* 18:2081–2092  
959 Tajima R, Matsumoto Y, Si H, Irikura K (2013) Comparative study on scaling relations of source parameters for  
960 great earthquakes in inland crusts and on subducting plate boundaries. *Zisin* 66:31–45  
961 Thingbaijam KKS, Mai PM, Goda K (2017) New empirical earthquake source-scaling laws. *Bull Seismol Soc*  
962 *Am* 107:2225–2246. <https://doi.org/10.1785/0120170017>  
963 THIO HK, SOMERVILLE P, ICHINOSE G (2007) Probabilistic Analysis of Strong Ground Motion and  
964 Tsunami Hazards in Southeast Asia. *J Earthq Tsunami* 01:119–137.  
965 <https://doi.org/10.1142/s1793431107000080>  
966 Wang Y-J, Chan C-H, Lee Y-T, et al (2016) Probabilistic seismic hazard assessment for Taiwan. *Terr Atmos*  
967 *Ocean Sci* 27:325–340  
968 Weatherall P, Marks KM, Jakobsson M, et al (2015) A new digital bathymetric model of the world's oceans.  
969 *Earth Sp Sci* 2:331–345  
970 Wells DL, Coppersmith KJ (1994) New empirical relationship between magnitude, rupture length, rupture width,  
971 rupture area, and surface displacement. *Bull Seismol Soc Am* 84:974–1002  
972 Youngs RR, Coppersmith KJ (1985) Implications of fault slip rates and earthquake recurrence models to  
973 probabilistic seismic hazard estimates. *Bull Seismol Soc Am* 75:939–964  
974  
975

## 976 **Statements & Declarations**

977

## 978 **Funding**

979 The present study was carried out within the frame-work of the project "Tsunami and Seismic hazard  
980 assessment for the Makran region." Funding for this project was provided by the Plan and Budget Organization  
981 of the Islamic Republic of Iran (PBO).

982

## 983 **Competing Interests**

984 Not applicable

985